



Norwegian University
of Life Sciences

Master's Thesis 2022 30 ECTS

Faculty of science and technology

Practical Applications of Mineral Detection Through Remote Sensing

**Anders Idar Risan Karlsen & Hans Vebjørn
Nordhagen**

Geomatics – Maps, satellites and 3D modelling



Contents

Abbreviations	4
Acknowledgements	4
Abstract	5
Abstrakt	6
1 Motivation	8
2 Intro	10
2.1 Hyperspectral imagery	10
2.2 Radiance And Reflectance	13
2.3 Atmospheric Corrections	14
2.4 Key Quality Parameters And Calibration Of Hyperspectral Imaging Systems	14
2.4.1 Spectral And Spatial Resolution	14
2.4.2 Keystone	15
2.4.3 Smile	16
2.5 Geology	17
2.5.1 XRF	18
2.5.2 REE's And Neodymium	19
2.6 Data Formats	20
2.6.1 HDR Format	20
2.7 Image Structures	21
3 Data Collection	22
3.1 Sensors	22
3.1.1 Cameras	22
3.1.2 Lidar	24
3.1.3 XRF	25
3.2 Data Acquisition Overview	26
3.3 Initial Field Exploration (XRF) [1]	26
3.4 Lab analysis	28
3.4.1 Collecting Samples [3]	28
3.4.2 Scanning Samples [4]	29

3.5	Field	31
3.5.1	Field Intro	31
3.5.2	First Field Data Collection With NEO [2]	33
3.5.3	Second Field Data Collection With NEO [6]	34
3.6	Data Processing	35
3.7	XRF Lab [5]	37
4	Software Development	39
4.1	The functionality of HyperAnalysis	40
4.2	User Interface	42
4.3	Hyperspectral Data Analysis - Hylite	44
4.3.1	Richardson-Lucy deconvolution	44
4.3.2	Hylite Classification Process	45
4.3.3	Hylite Modifications And Output	48
5	Results	50
5.1	Initial Field Exploration (XRF) [1]	50
5.2	First Quarry-Scan [2]	51
5.3	Lab Samples [4]	53
5.4	Lab Samples XRF Validation [5]	57
5.5	Second Quarry-Scan [6]	57
5.6	Processing	61
6	Discussion	63
6.1	Classifications Aspects, Potential For Machine Learning	63
6.2	Can REE Classification Based On Hyperspectral Imaging Be Integrated Into The Mining Industry?	64
7	Conclusion	65
7.1	Further Research	66

Abbreviations

NEO	Norsk Elektro Optikk AS
Hyspex	Department in Norsk Elektro Optikk
REE	Rare earth elements
MWL	Minimum wavelength mapping function
HIS	Hyperspectral Imagery
GUI	Graphical User Interface
LiDAR	Light detection and ranging
GSD	Ground sample distance
CPU	Central processing unit
SSD	Solid State Drive
RAM	Random Access Memory
MB	Mega byte
GB	Giga byte
TB	Tera byte
WR	Calibrated white reference panel
VNIR	Visible and near-infrared
SWIR	Short wave infrared

Acknowledgements

This thesis marks the end of our master's degree in geomatics at the Norwegian university of life science. There are no direct cooperation partners, however this thesis would never have happened without support and help of many individuals and firms whom we would like to thank. We are two silly boys who have had the best support team we could ever have asked for.

Firstly, we would like to thank Magne Martinsen who has helped us from the very beginning. you are the reason we would ever consider doing an assignment in this genre. If I am not mistaken, you are the one who came up with the idea for the thesis. . . Thank you for the many talks and whiskey recommendations throughout the whole process. We really could not have gotten a better guide! We also want to thank Lundhs who were very kind and allowed us to use their quarry in the thesis.

We must also thank our trip leader Friederike Körting and Norsk Elektro Optikk who has given us opportunities we never thought we would have. Thank you NEO for lending us Friederike who held our hand the entire time, and helped us collect data with state of the art sensors from NEO. We would be lost in this thesis without you Freddi. . . Thank you so much for being the greatest trip leader in this geological mess we put ourselves in.

Thirdly we must thank Dagrún Aarsten who has been a great supervisor, who pushed us ahead and gave us many tips and tricks. You are unquestionably one of the coolest persons we have met during our studies. You even helped these utakknemilige beistene with their MSc thesis, thank you DGRN. We must also thank Ivar Maalen-Johnsen who had been guiding us through the studies and in the early stages of the MSc. You have been the father of geomatics the whole way!

Fourthly, we must thank NIBIO and specifically Pierre-Adrien Rivier who entrusted us with their XRF unconditionally (what were you thinking?!). Getting ahold of a XRF started a snowball effect which made this thesis possible.

Last but not least we want to thank our fellow students who have travelled this path with us. It has been a blast, may we meet again.

Abstract

There is a global demand for rare earth elements (REEs), as they are a cornerstone in many industries. REE demand is expected to grow tremendously due to raw material constraint combined with the transition to a carbon neutral economy. The road to having a carbon neutral world is reliant on many environmentally friendly inventions that are heavily dependent on REEs. The recent conflict between Russia and Ukraine has affected the global supply chain and the need for countries to be more self-reliant is more apparent. Therefore, more local solutions should be explored.

Mapping of rare earth elements with hyperspectral imagery has been proven effective in research. However, the technique has yet to be demonstrated at quarries. This MSc project investigated potential procedures that could streamline the process of mapping REEs in field. The aim was also to determine whether a discontinued quarry in Larvik Norway had high enough concentration of REEs to be mapped by hyperspectral imagery. The element of interest in this study is neodymium since it has prominent spectral features and can be used as a proxy for REEs occurrences since REEs often occurs together. By using cameras from HySpex (VNIR1800, VNIR3000) it was possible to identify potential neodymium occurrences both in lab and in field. The results showed that the concentration of neodymium is high enough to be mapped by hyperspectral sensor. And that the process of classifying neodymium was possible to streamline even with a great deal of data. The process also has the potential to be refined and scaled up.

Abstrakt

Sjeldne jordarter (REE) er en essensiell del av mange industrier noe som medfører en stor global etterspørsel. Det er forventet en enorm økning i etterspørsel av REE grunnet råvaremangel og overgangen til en karbon-nøytral økonomi. Veien til å bli karbonnøytral er avhengig av mange miljøvennlige oppfinnelser som også belager seg på REEs. Den nåværende konflikten mellom Russland og Ukraina har påvirket den globale forsyningskjeden og mange land kjenner behovet for å være selvforsynt i større grad enn før. Derfor bør man utforske mer lokale løsninger.

Kartlegging av sjeldne jordarter med hyperspektrale kameraer har vist seg å være effektivt i forskning. På tross av dette har det ennå ikke blitt iverksatt i den aktive driften hos steinbruddene. Denne masteroppgaven har utforsket potensiale for å effektivt kartlegge REE i felt, samt om et steinbrudd i Larvik hadde høy nok konsentrasjon av REE til å bli kartlagt av hyperspektrale sensorer. Hovedelementet i denne oppgaven er neodym da den har tydelige spektrale egenskaper og kan brukes som en indikator på andre sjeldne jordarter. Dette kommer av at sjeldne jordarter ofte forekommer sammen. Ved å bruke kameraer fra Hypex (VNIR1800, VNIR3000) var det mulig å identifisere neodymforekomster i lab og felt. Resultatene viste at det var høy nok konsentrasjon av neodym til at de hyperspektrale sensorene klarte å fange det opp. Det viste seg også mulig å effektivisere klassifiserings prosessen, selv med store mengder data. Rutinen har potensiale til å bli mer raffinert og skalert opp.

1 Motivation

Hyperspectral imagery (HSI) is a remote sensing technique that excels in identifying and differentiating surface material's ability to absorb and reflect electromagnetic energy. This can be used to identify elements, molecules and in the context of geology minerals, given high enough concentration and occurrence. Some elements show element-specific absorption features, REE elements are part of this group. The purpose of this study is to see whether it is possible to use hyperspectral imagery to effectively map rare earth elements at a discontinued quarry in Larvik, Norway. The aim is also to determine whether the REE concentration in the quarry is high enough to be mapped by HSI. Prior studies have shown the possibility of identifying REEs using hyperspectral sensors . However, the technique has yet to be put in practice at quarries, exploration from UAV and tripod have been tested but not industrialized (Boesche et al. 2015; Turner, Rivard, and Groat 2018; Herrmann 2019; Booysen et al. 2020). A challenge with identifying small occurrences of minerals is the need for high geometric and spectral resolution. This results in a great deal of data, even for relatively small areas. In our study, the element of interest is neodymium. Neodymium (Nd) has prominent spectral features and can be used as a proxy for REEs occurrences since REEs often occurs together (Boynton 1984). Studies have also shown that Nd can be detected in rocks up to a lower concentration limit of 300 PPM (Rowan, Kingston, and Crowley 1986).

There is a global demand for REEs, as they are a cornerstone in many industries. Demand is expected to grow up to sevenfold (IEA 2021) due to raw material constraint combined with the transition to a carbon neutral economy (Boissenin 2021; Ilankoon et al. 2021). There are many environmental-friendly inventions which are reliant on REEs, but the most pressing is the potential electrical vehicle revolution. According to Xu et al. 2020 it is estimated that there will be over 1 billion electrical cars by 2050, with a production of 100 million per year. This would require more green-energy production. Europe gets about 98% of its needs of REEs from China (Boissenin 2021). The conflict between Russia and Ukraine, as well as Covid before have greatly affected the global supply chain. Countries need to be more self-sufficient when the supply chain is unpredictable due to an increase in geo-political risk. Therefore, a focus for Europe and Norway will be the exploration of local deposits of raw materials critical to the planned energy transition. A

critical step in that exploration, is the ability to map and quantify potential source areas effectively. Hyperspectral mapping of REE-enriched areas in established mines like the one presented in this work could help with deposit modelling, selective extraction of material, sorting of REE rich material into processing chain of the quarries.

2 Intro

This chapter will cover basics principles about the theory and technology that creates the foundation for this thesis.

2.1 Hyperspectral imagery

Hyperspectral imagery also called imaging spectroscopy is a method of remote sensing that maps a wide part of the electromagnetic spectrum, instead of just the parts that are visible to the human eye. Hyperspectral imagery refers to the large number of narrow, consecutive, overlapping bands, enabling a high spectral resolution and detail when analyzing spectra and the ability to resolve narrow spectral absorption features of 15nm width (Shukla and Kot 2016).

Hyperspectral cameras record the full spectrum of each pixel in the image within a given spectral range and with a given number of spectral channels. This is done by measuring the amount of light per wavelength that is being collected by the sensor. The spectral range and the number of spectral channels is dependent on the camera's specifications. Pushbroom and full frame are the two main types of hyperspectral cameras. The full-frame version records the entire image frame or scene one wavelength range per frame. Pushbroom cameras record in a line-by-line fashion, recording all wavelength ranges per line at once and only then moving to the next line. The output of the hyperspectral camera acquisitions can be represented as a data cube, often called a hypercube, or a hyperspectral data cube. The spatial information is stored in the x- and y-axis, while the spectral information is stored in the z-axis (see Figure 1)

The large number of narrow spectral bands collected by a hyperspectral camera allow the sensor to measure the interactions between materials and electromagnetic light precisely (Boesche et al. 2015). Matter interacts with incoming radiation by absorbing, reflecting or transmitting the incoming energy. This is material specific and these interactions are wavelength dependent. The electromagnetic light reflected by a material surface therefore contains information about the absorption and reflectance attributes of the matter. A spectrum collected over a material surface will show wavelength dependent changes in reflectance, exhibiting local maxima and minima within

the spectral curve. This is called a spectral signature, and essentially works as a fingerprint for the material reflecting the light.

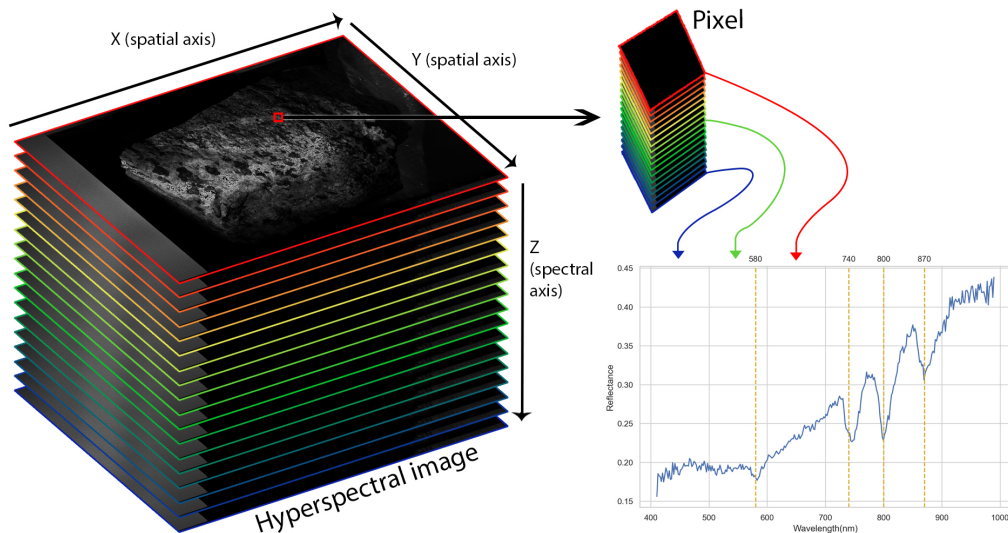


Figure 1: Illustration of hyperspectral data cube

Spectral signatures exhibit features which are distinct to the given material because of their elemental, molecular or crystalline characteristics. There are five causes for elemental absorptions (Boesche et al. 2015): (1) crystal field effects, (2) charge-transfers, (3) color center, (4) transition to conduction bands and (5) vibrational transitions. The features are located in the spectrum where the material either absorbs or reflects a lot of electromagnetic light. This results in local peaks and dips in the spectrum. Since there can be more than one material in each pixel, the dip or peak of the features is therefore determined by the concentration of the material in the pixel (Herrmann 2019). Some materials share features which will then superimpose the feature. However, materials can also cancel out each other's features as well. These features can be located anywhere on the electromagnetic spectrum. However, some parts of the light spectrum are more difficult to work with than other. The atmosphere absorbs some of the light emitted from the sun stronger at certain parts of the electromagnetic spectrum (Widén and Munkhammar 2019). While the sun also emits its energy stronger at certain areas of the spectrum. This combination makes it harder to separate features from noise

at the higher wavelength part of the spectrum when using the sun as a light source due to the lower emitted energy. To get good data in field with the sun as light source, it is highly recommended to use the VNIR spectrum. The VNIR spectrum goes from 350nm to 1000nm, and is more noise resilient than the SWIR spectrum, which goes from 1000nm to 2500nm. The materials in focus must therefore be identifiable in the VNIR spectrum.

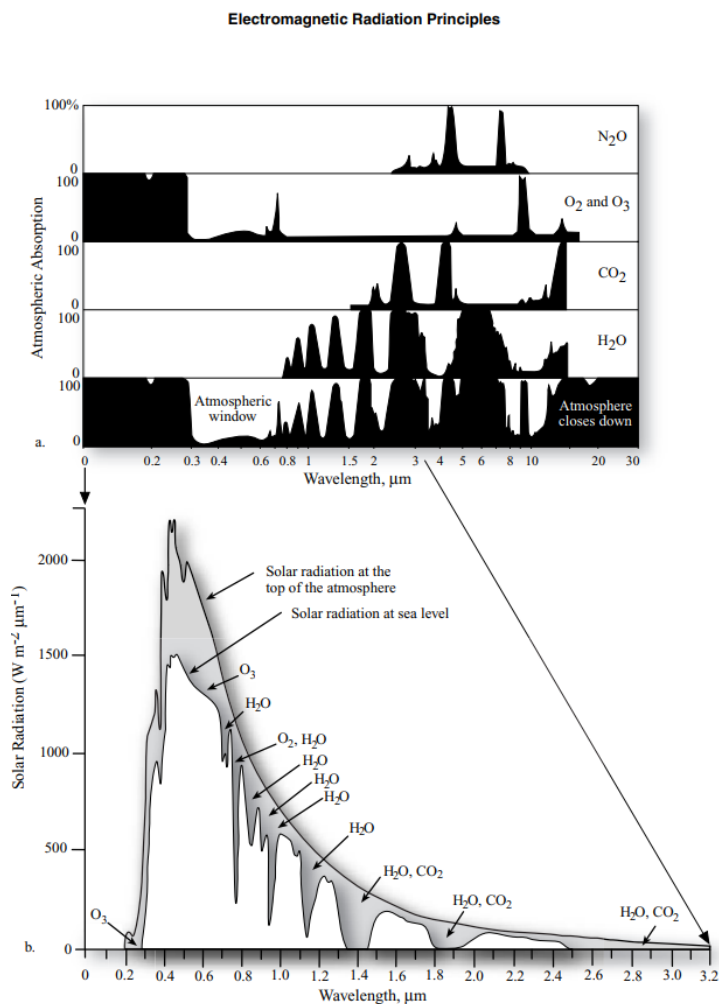


Figure 2: Figure : The solar irradiation and atmospheric absorption from multiple molecules. (Jensen 2014)

2.2 Radiance And Reflectance

Radiance is a variable which is a metric of how much electromagnetic energy enters the detector of a remote sensing instrument. When the measurement is performed outdoors the light has to pass through the atmosphere, which scatters some of the light (Gilabert, Conese, and Maselli 1994). This results in a decrease in the light's intensity and radiance. However, some of the scattered light enters the sensor and is observed as radiance of the target and introduces noise to the measurement. It is quantified in $\frac{\text{watt}}{\text{sr}/\text{m}^2}$. Where watt is the intensity of the light, Sr is the steradian which is the planar angle of the light, and m² is the area which is hit by the light.

Reflectance is a physical property of the matter being observed. It is the proportion between the light that hits the observed material, and the light caught by the sensor. It has no units but is often measured as a fraction of 1 or 0 to 100%. Which describes the percentage distribution of the total light absorbed by a band in a specific pixel.

There are several factors when scanning outside that will affect the reflectance. The challenge is inhomogeneous scenes with areas of shadow, less light and sharp edges. A way to compensate for these factors is to do a “joint Illumination correction” (S. Thiele et al. 2021), which uses 3D data from lidar, viewing direction and sky view factors and yield “true reflection”. If one only compensates for the atmospheric effect and solar illumination; this yields the “apparent reflectance” of surfaces. Which varies from true reflectance since one has not dealt with the shadow and directional effects. However, in many cases apparent reflectance allows for satisfactory analysis. Apparent reflectance will be referred to as “reflectance” later in the thesis since there is no “true” reflectance used in our experiments.

2.3 Atmospheric Corrections

To accurately analyze surface material using HSI in the field, one must remove atmospheric scattering effects (B.-C. Gao et al. 2009; Rani, Mandla, and Singh 2016). It is essential when transforming data from radiance measured by a sensor to reflectance. This process is called atmospheric correction and there are essentially two methods, empirical and model based. There are numerous algorithms and practices within the two main methods. Empirical is a scene-based method and uses internal pixel-values to calculate relative reflectance. Model based uses external information to compensate and rectify for the atmospheric absorption. A combination of the two methods is to use “field truths” in form of using reference panels. One then uses the empirical method and use the pixels from the calibrated, known reference white-panel to calculate the reflectance.

2.4 Key Quality Parameters And Calibration Of Hyperspectral Imaging Systems

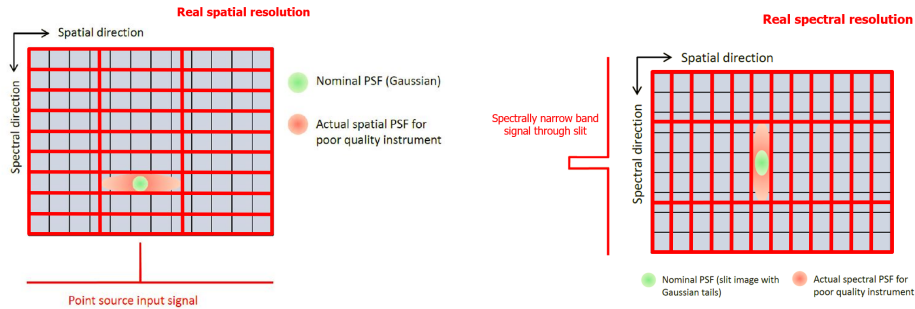
2.4.1 Spectral And Spatial Resolution

Spatial resolution is the level of geometrical detail, that can be extracted from an image. It is measured by the number of pixels that accurately captures these details in the image. Which means that spatial resolution is restricted by the optical system of the sensor. However, the number of pixels is not the same as spatial resolution due to the point spread function (PSF). PSF describes the inevitable dispersal of energy, when passing through an optical system to a certain point in the image plane (Gu, 2000). (See Figure 3a)

A PSF Transforms a theoretical point into a “blur circle”, which may result in energy dispersing into neighboring pixels as is shown in the figure below (Figure 3a). This would mean that an image with 100 nominal pixels, and a PSF with the width of 2 would result in an image with $100/2 = 50$ effective pixels.

Spectral resolution is the level of spectral detail that can be extracted from a band. Narrower bands are able to resolve finer spectral details in the acquired spectral information, collecting spectral information at a higher precision. The spectral response function (SRF) is an important parameter of a hyperspectral imaging system. It describes where a sensor allocates the

energy from a narrow spectral signal. Same as the PSF, the SRF can cause the collection of energy leaking into neighboring bands (Z. Gao et al. 2016). This results in a lower spectral resolution, as energy from more than 1 band is collected within one spectral band of the sensors, causing a loss of resolution. See Figure 3b



(a) Visualization of PSF from NEO and how electromagnetic light can leak into neighboring pixels (b) Visualization of SRF from NEO and how spectral values can leak into neighboring bands

Figure 3: Illustrations of spatial and spectral resolution

2.4.2 Keystone

Spatial misregistration is also called keystone (Bakker, Werff, and Meer 2019). It is a magnification variation which can cause bands to be allocated to the wrong pixels within the same scene. Keystone can drastically change spectral signatures, especially in inhomogeneous scenes. And render the classification results to be useless.

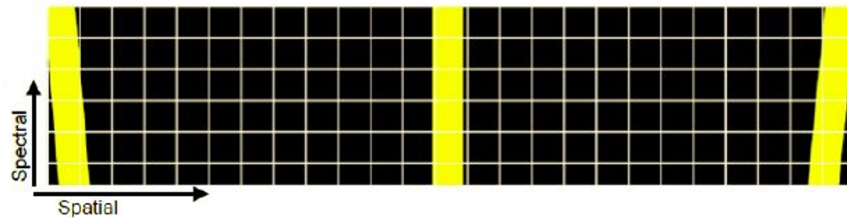


Figure 4: Illustration of keystone from NEO. How the bands are potentially placed in the wrong pixels at the edges of the image sensor.

2.4.3 Smile

Spectral misregistration is a spectral distortion, and is also called the smile effect (Bakker, Werff, and Meer 2019). The position of the spectral band varies with the spatial position of the pixels. There are several shapes that spectral misregistration can take, but often it is a bending across the field of view in the image plane. The smile effect is caused by distortion in the optics or dispersal elements. However, misalignment of the slit and sensor may also cause a spectral misregistration (see Figure 5). Spectral misregistration can make it impossible to detect narrow spectral features, even with a very small smile.

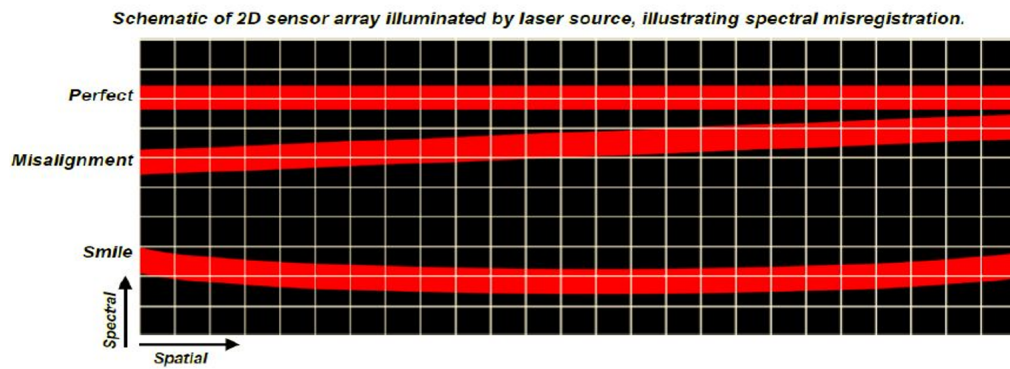


Figure 5: Illustration of spectral misregistration from NEO. This is in the image sensor (sensor array)

2.5 Geology

The quarry studied (“Vevja”) is situated in a range of peculiar monzonitic rocks in the southern part of the Oslo province (Heldal and Dahl 2013). The Oslo province was developed in the late Carboniferous and early Permian and consisted of pluton from monzonite to nepheline syenites (Neumann et al. 2004). Veins are of great interest, since they can be seen in the quarry face and might contain REEs (Goodenough et al. 2016).

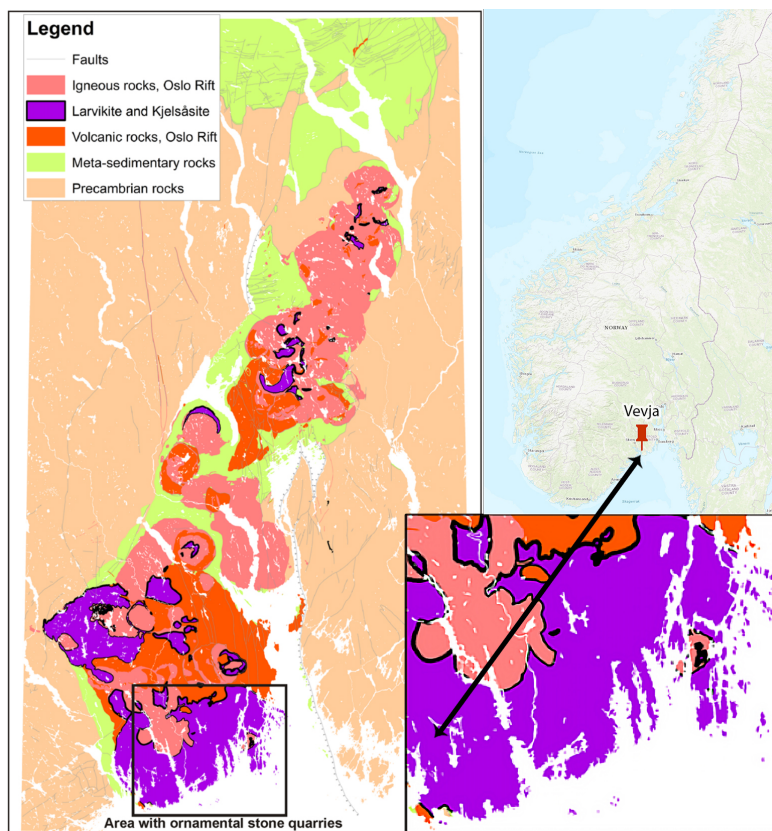


Figure 6: Caption

This thesis does not study the geological and mineralogical aspects in detail, but aims to look at the topic from an application perspective. The main goal is to figure out if Nd can be detected by hyperspectral cameras in the quarry. For more in depth information about the geology take a look at (Sunde, Friis, and Andersen 2019).



Figure 7: Overview image of Vevja

2.5.1 XRF

The principle of X-Ray fluorescence spectrometry is based around subjecting elements to high energy X-ray-radiation and measuring the radiation that occurs when electrons change orbit. When atoms are exposed to high x-ray energy it excites the electrons to higher energy electron shells. When the radiations stream ends the electrons returns to their original shells and emits a precise roentgen-radiation which works as a fingerprint for the atom and is element-specific (Crocombe, Leary, and Kammrath 2021). This allows the scanning of material without touching or damaging the samples. The results are a table which describes the distribution of elements in the sample and each elements concentration in the form of parts per million. The values generated from a handheld-XRF are different from lab-XRF as they are probably not calibrated systems. The values are therefore relative and not absolute.

2.5.2 REE's And Neodymium

Rare earth elements also called lanthanides are a collective definition of 16 elements, with atomic number 57 to 71. They are elements that predominantly occur together in geological settings (Boynnton 1984).

Neodymium is a REE and has atomic number 60. It has many practical applications such as being an essential part of the optic industry and in the creation of modern magnets (Jackson and Christiansen 1993) and more. Neodymium has numerous absorption features in the VNIR spectrum between 400-1000nm. The most apparent features appear around 580, 740, 800 and 870 nm (Boesche et al. 2015; Herrmann 2019). The absorptions for REEs are assumed to be caused by electronic field transitions (Rowan, Kingston, and Crowley 1986). However, there has been research that have indicated that the absorption bands neodymium is also caused by vibrations (Herrmann 2019).

It is possible to measure the concentration, based on the absorption depth of the spectral features. And research done by (ibid.) shows that the strongest correlation between absorption depth and REE concentration is demonstrated at concentrations below 10%. For neodymium to be visible in HIS the minimum concentration has to be 300 PPM (Rowan, Kingston, and Crowley 1986).

There are several factors that will greatly affect the process of mapping neodymium with HIS, a major one is the concentration of iron. Iron absorption bands will obscure neodymium's spectral signature (Boesche et al. 2015; Herrmann 2019) and make classification more difficult. Two measures taken in (Boesche et al. 2015) to better classification: (1) average across multiple images, (2) use of the Richardson-lucy algorithm. These are techniques that will not be used for the final product of this thesis, due to good results from other techniques. Which is why the procedures done in this thesis are somewhat novel.

2.6 Data Formats

2.6.1 HDR Format

The HDR image format also known as the “Radiance format”, is a raster image that is built up by an “.hdr” and “.pic” file. “.pic” files can also have the file extension “.img”. “The file wrapper consists of a short ASCII header, followed by a resolution string that defines the image size and orientation, followed by the run-length encoded pixel data” (Reinhard et al. 2006).

The ENVI HDR format is structured similarly to a standard HDR file. The header contained in the “.hdr” file mostly describes the data contained in the “.pic” file. This header often contains a “description” that normally describes information that is not directly related to the data in the file itself, but how the data was obtained. Descriptions can contain information like what lens was used or the serial number of the camera. Other elements that are defined in the header are directly related to the data, I.e., how many bytes are used to represent each value in the “.pic” file. Some of the elements defined in the header are the number of lines, samples and bands; interleaving type and data type; wavelengths and wavelengths units. The “.pic” file is a flat binary raster that contains the actual values for each band in each pixel. The values in the “.pic” file is ordered in one of three interleaving types that is also defined in the “.hdr” file.

2.7 Image Structures

To store pictures in a flat binary stream, one must define an interleaving type. There are three typical types (Schowengerdt 2007): Band sequential (BSQ), band interleaved by line (BIL) and band interleaved by pixel (BIP).

- BSQ stores the values by defining the bands one by one. Here it lays out the entire first band in order, then the second, third etc.
- BIL takes the first line of the picture and lays out the values for all the bands that are in that line. Then it jumps to the second line and lays out all the bands, then the third etc.
- BIP lays out all the values in each pixel before it goes onto the next pixel.

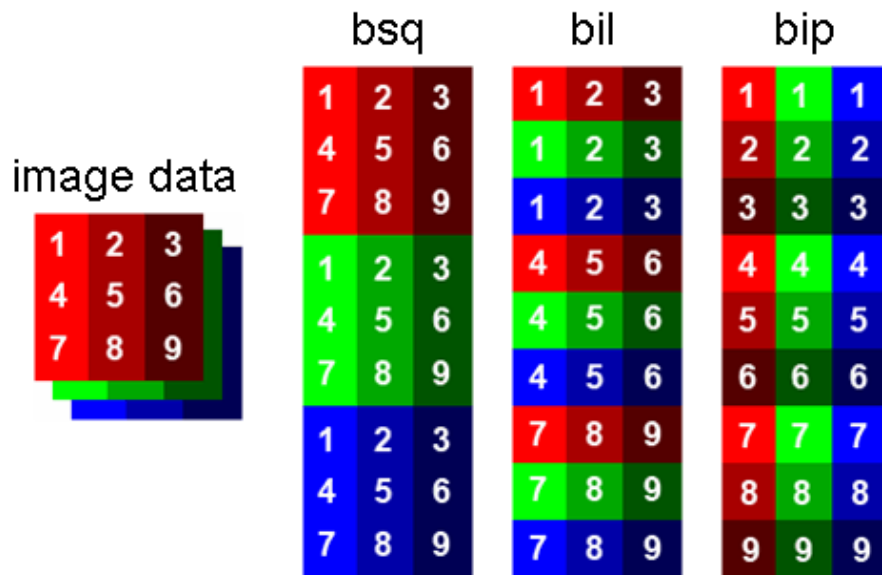


Figure 8: The different interleaving types (<https://bitbucket.org/hu-geomatics/enmap-box-idl/wiki/Data%20Format%20Definition>)

3 Data Collection

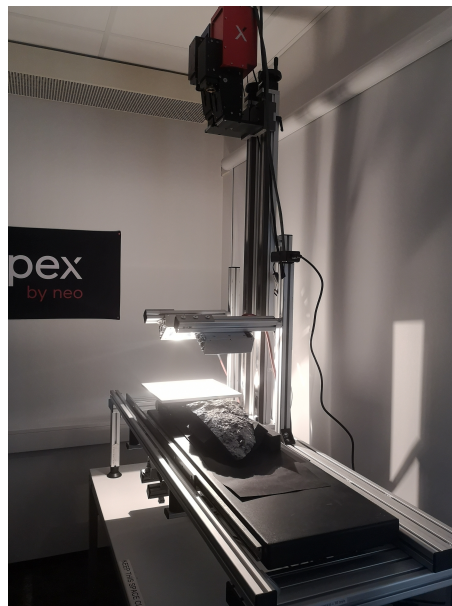
3.1 Sensors

The sensors used for data acquisition consist of three different HySpex cameras, a lidar and an XRF. The HySpex cameras were used to collect hyperspectral data in lab and field. Lidar was used as a supplement to the hyperspectral camera and was used in field. The XRF served as an exploration and validation tool to identify areas of interest.

3.1.1 Cameras



(a) Hypspx VNIR1800 in field



(b) Hypspx VNIR3000 and SWIR384 in the lab

Figure 9: Cameras in field and the lab

Hypspx is an industry-leading brand of hyperspectral cameras produced by Norsk Elektro Optikk AS (NEO). NEO produces top-of the line quality cameras with high spectral and spatial resolution. HySpex cameras are pushbroom based and collect images in a line-by-line fashion. This means that the sensor is reliant on some sort of external spatial transition to collect

data. The camera was mounted on a tripod with rotation stages in field with a motorized tripod head rotating the camera line-by-line during image acquisition. In the lab, the camera was mounted above a conveyor belt that moved the samples at a constant speed below. The camera specification of the cameras used in this project are listed in Table 1.

Main specifications	VNIR1800	VNIR3000	SWIR384
Spectral range	400 – 1000nm	400 – 1000nm	930 – 2500nm
Spatial pixels	1800	3000	384
Spectral channels	186	300	288
Spectral sampling	3.26 nm	2.0nm	5.45nm
FOV	17°	16°	16°
Pixel FOV across/along*	0.16/0.32 mrad	0.096/0.32 mrad	0.73/0.73 mrad
Bit resolution	16 bit	12 bit	16 bit
Noise floor	2.4 e-	2.37 e-	150 e-
Dynamic range	20000	11000	7500
Peak SNR (at full resolution)	255	170	1100
Max speed (at full resolution)	260 fps	117 fps	400 fps
Power consumption	30 W	30 W	30 W
Dimensions (l–w–h)	39 – 9.9 – 15 cm	39 – 9.9– 15 cm	38 – 12– 17.5 cm
Weight	5.0 kg	5.0 kg	5.7 kg
Camera Interface	CameraLink	USB3	CameraLink

Table 1: Hyspex VNIR1800/3000 and SWIR384 sensors parameters. Collected from (www.hyspex.com)

3.1.2 Lidar

The terrestrial lidar used is a single mirror terrestrial lidar with an integrated GPS. It uses a rotating mirror to scan 300° vertically and 360° horizontally. Specification of the Lidar system that was used can be found in Table 2.



Figure 10: FARO X 130 HDR in field

Specifications	FARO X 130 HDR
Power supply	19V(External), 14.4V(Internal battery)
Power consumption	40W/80W
Battery life	4.5 hours
Ambient Temperatur	$5^\circ - 40^\circ\text{C}$
Weight	5.2 kg
Size	240 x 200 x 100mm
Unambiguity interval	30m
Range Focus	0.6m - 30m indoor or outdoor with upright incidence to a 90% reflective surface
Measurement speed (pts/sec):	122,000 / 244,000 / 488,000 / 976,000
Ranging Error	$\pm 2\text{mm}$
FOV	$300^\circ / 360^\circ$
Max Vertical scan speed	5820rpm / 97Hz
Wavelength	1550nm
Beam divergence	Typical 0.19 mrad (0.011°) (1/e, halfangle)
Beam diameter at exit	Typical 2.25 mm (1/e)
Laser class	Laser class 1

Table 2: FARO X 130 HDR sensor parameters

3.1.3 XRF

The wonderful people at NIBIO allowed us to borrow a handheld XRF for the duration of our thesis. The handheld XRF uses X-ray to map elements. The concentration of the detected elements is given in parts-per-million(ppm) along with a standard deviation if applicable. After contacting the manufacturer, we were informed that it has a lower detection limit (LOD) of around 200 ppm, where it can detect an element with statistical significance. We were also informed that it has a limit of quantification (LOQ) of 600ppm and that we would have ca. 20% precision at the 1000ppm level. LOQ is the limit where an element can be quantified with a given measure of certainty.



Figure 11: Image of Spectro xSORT

The XRF was used in field and in lab as a tool for both finding interesting areas to scan hyperspectrally and for validation of the scanned areas. Specification of the XRF Spectro xSORT can be found in Table 3.

Technical Data	Spectro xSORT
Operating voltage range	9.0 – 12.6 V
X-ray tube	h (opt. W) anode, up to 50 kV, up to 125 μ A, max. 2.5 W
Total power during the analysis	11 W
Total power in the standby mode	6 W
Operating range (permissible ambient temperature)	10 – +45 °C; 14 – 113 °F

Table 3: xSORT SPECTRO sensor parameters

3.2 Data Acquisition Overview

The data acquisition was done throughout the winter of 2021 and spring of 2022 and was made up of more than six individual instances of data collection. Firstly, the initial exploration of the promising area using a handheld XRF. Secondly, was the first scan of the quarry with NEO’s hyperspectral HySpex cameras and the Lidar. The third was acquiring rock samples for scanning in NEO’s lab. Fourthly, scanning the rock samples at the NEO lab in Oslo. Fifthly, was validating the sample results using an XRF-lab. The sixth and final collection was the second hyperspectral scan at the quarry with NEO.

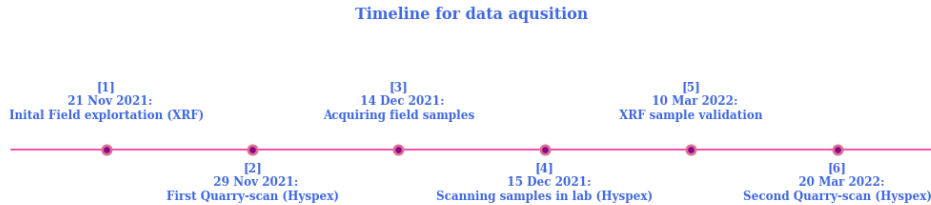


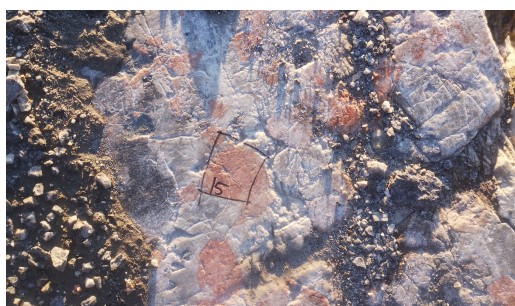
Figure 12: Timeline for all the instances of data acquisition

3.3 Initial Field Exploration (XRF) [1]

A prerequisite to identify Neodymium with a hyperspectral camera, is that the concentration of neodymium is high enough to separate it from other minerals with no or little Nd content. To establish whether the concentration in the quarry was high enough, manual point measurements were done at the wall with an XRF. 17 spots were marked with tape or marker across two areas in the quarry that were to be scanned with the XRF. The points were selected in conjunction with the quarry’s head geologist (Dr. Magne Martinsen) who has domain knowledge of quarries in the area. All the measurements lasted 60 seconds, and some areas got measured more than once. Since the XRF is handheld, it’s hard to get spatially precise measurements and the marked areas are larger than the actual measured area.



Figure 13: Labeling of the spots scanned with the XRF in the initial exploration of the quarry



(a) Spot 15



(b) Spot 16 & 17

Figure 14: Labeling of spots scanned, which are not on the wall

3.4 Lab analysis

3.4.1 Collecting Samples [3]

The samples that were collected originate from the same wall that got scanned in both the first and second field data collections with NEO [2][6]. We brought tools that could cut and break off parts of the wall so that the interesting areas could be taken to the lab. However, since the wall only has one sharp edge which is at the west side, it became hard to chop out stone shards from the interesting areas. Due to this, we found it was easier to collect rocks which had fallen off naturally. Luckily the interesting area had many shards that had already fallen off. Five samples were collected from the vein in Figure 15a, and two samples from another wall. A manual scan with the XRF was done on the samples to see if the concentration of Nd was satisfactory. In the end we opted to bring samples that had been measured as both low and high concentration to compare them with each other in the lab.



(a) The area from which the samples got collected (b) The samples collected from the wall

Figure 15: Sample collecting from the quarry ("Vevja")

3.4.2 Scanning Samples [4]

The camera setup used in the lab consists of two Hypspx cameras. One which operates in the visible light and near infrared spectrum (VNIR-3000) (400-1000nm), and the other in the shortwave infrared spectrum (SWIR-384) (1000-2500nm). The VNIR camera has a resolution of 3000 pixels and a field of view (FOV) of 36.64 cm using a 1m lens. This means that the VNIR image GSD equals 0.1 mm. The SWIR camera has considerably lower resolution with 384 pixels and a FOV of 28.76cm, which equals a GSD of 0.75mm using the 1m lens. The length of the scan (collected frames of the image) was adjusted to the sample size.

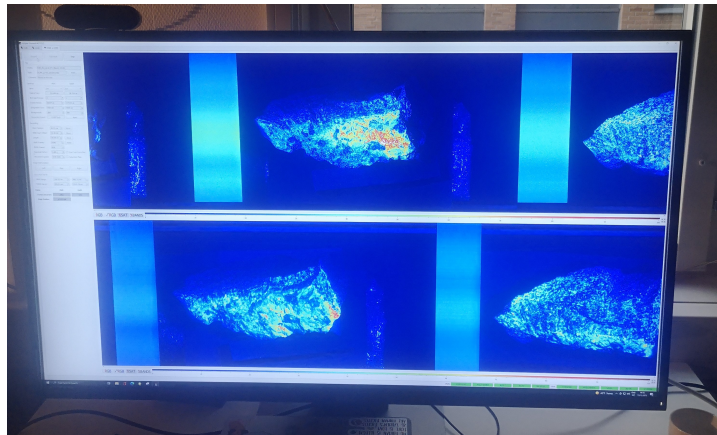


Figure 16: Saturation image representation of a sample from the lab

For the data collection in the laboratory, 7 samples from the quarry were brought to HySpex's lab where we were lucky enough to be helped by Dr Friederike Körting. By identifying interesting surfaces on the rocks and tilting them in such a way that the sample would be most homogenously illuminated, it was possible to map most of the sample's surfaces. The integration time of the cameras was adjusted as to not oversaturated the sample surface. If ideal illumination cannot be achieved over the full sample surface the sample was scanned twice to change the angle of the sample towards the light and illuminate other areas of interest in the sample. Figure 17 shows the setup in the laboratory. Within each scan a couple of centimeters of the calibrated white reference panel were scanned for the reflectance retrieval. 8 scans were acquired in total. A saturation image representation of a scan from the data acquisition software screen is shown in Figure 16.

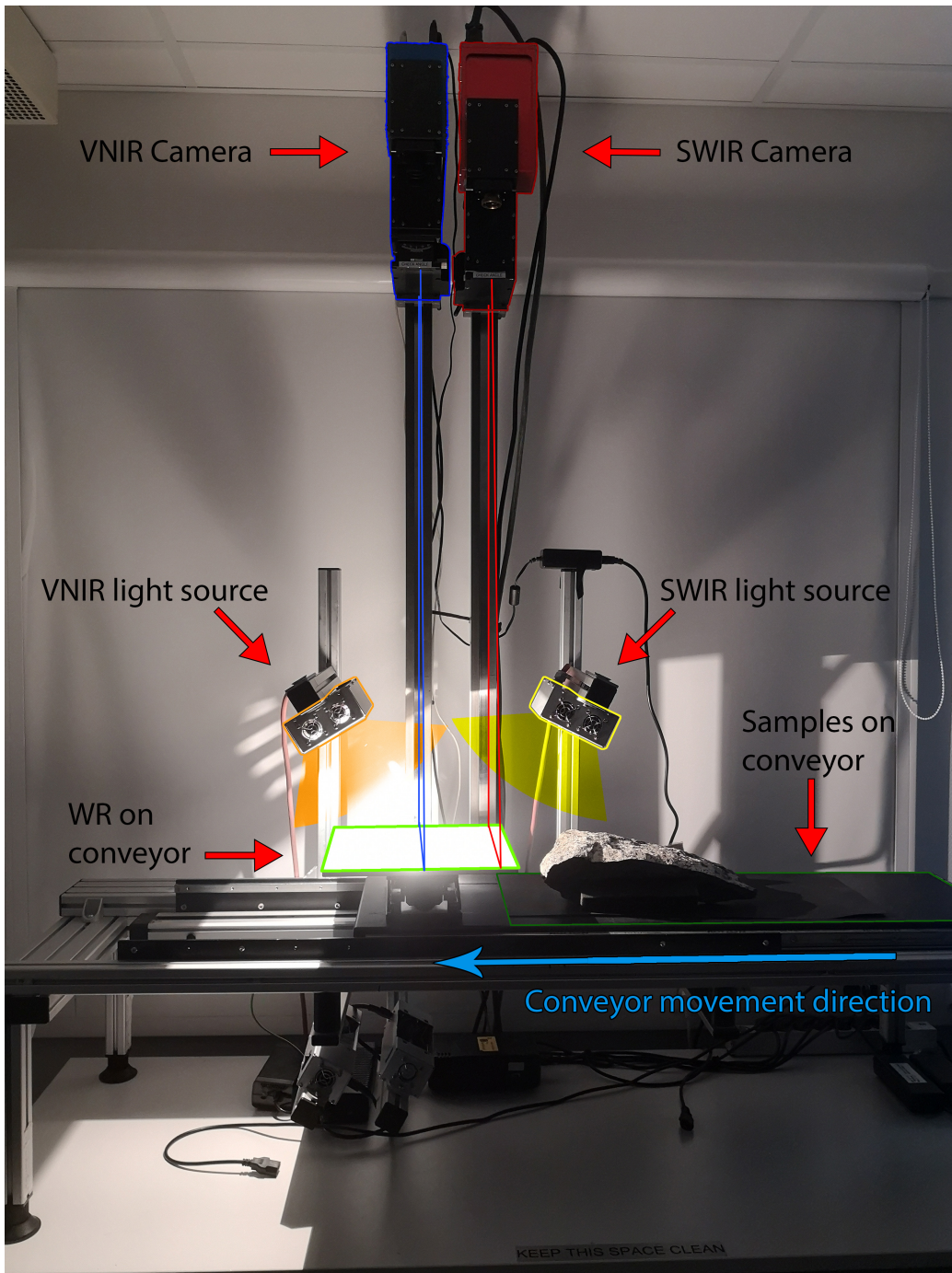


Figure 17: Image of the lab setup with illustrations

3.5 Field

3.5.1 Field Intro

For the field data collections, we were accompanied by Dr. Friederike Körting from NEO who helped us collect all the hyperspectral field data. The sensor used was a Hyspex VNIR1800. It is a pushbroom sensor with a spatial pixel length of 1800 pixels per line. It was mounted on a tripod with motorized rotation stages, which allowed us to rotate the camera head at a specific speed. The camera and the rig were controlled with a field computer and powered by a generator. The reflection panel used in the field was a calibrated panel of 50% reflectance (WR50) and reference foil of around 50% reflectance. WR50 was used on the first trip, and the foil was used in the second. The field setup can be visualized in Figure 19.



Figure 18: Overview of the quarry and the different walls that got scanned. Wall6 is further east and is not included in this figure.

The studied area of interest is a quarry ("Vevja") located in the south of Norway. It has earlier been mined for larvikite but is now inactive. The quarry walls face southwest and northwest and have many different levels. We scanned at total of six walls, five in the inactive quarry and one wall further east. The data collection was initially done in December 2021. However, due

to difficulties with the light conditions another trip was done in March of 2022. For the initial trip in December only two walls were scanned. This was due to the sun, and its low orbit in December. The walls scanned in December was wall1 and wall4, where wall1 was the focus. For the second trip wall 1,2,3,5 and 6 were scanned. The suns orbit in the middle of March gives substantially longer days and better sun conditions than in December. For the location of the walls see Figure 18.



Figure 19: Image of field setup with illustrations

3.5.2 First Field Data Collection With NEO [2]

The wall in focus, “wall1”, is faced south and slightly west. Since the data collection was done in December. The time with optimal light was shorter and the sun angle was considerably low, so it did not illuminate the entire wall. Therefore, it was critical to find the time which had the best sun angle towards the wall. This was done by downloading lidar data from “hoymedata.no” and running a simulation with the sun angle. This was done in «Quick Terrain Modeler v8.2.3» by Applied Imagery, which calculates the sun and shadow angle based on time and date. The time with best illumination was around 2 pm, based on the simulation.

Wall1 is approximately 12 meters tall, and 22 meters long. The hyperspectral rig was set up in two different distances from the wall, 13 and 23 meters using 9-13m and 13-23m lenses respectively. The calibrated white reference panel used in all the scans, was a WR50. Due to the snow on the ground, the saturation became somewhat of a problem. Wall4 was scanned later than wall1 and was only scanned from one distance.

To be able to backtrack and validate the data, the XRF was used to measure points on the walls that were marked with black tape. We measured a total of 7 points on wall1 and 14 points on wall4, with a measure time of 60 seconds.

The lidar was set up in three different positions on the main wall, and 2 different positions on wall2. Since the snow could interfere with the white reference spheres, they got placed on the wall. Used the “outdoor” settings, and used $\frac{1}{2}$ resolution, so that each scan took approximately 15 minutes. The lidar scans approximately 244 000 points per second in this exact setting.



Figure 20: Image from the first field day with the head geologist (Dr. Magne Martinsen).

3.5.3 Second Field Data Collection With NEO [6]

The same procedure was done to estimate the best time to scan wall1. This showed that between 1pm and 5:30pm the wall was to be fully illuminated if the sun conditions were good. The weather on the 20th of march had ideal sun conditions, no snow, and little to no clouds. This gave us time to scan multiple walls with good illumination. Five walls were scanned throughout the day. The WR also got swapped out for this trip to a foil WR. A major difference from the first field data collection, is that we had already analyzed the lab data before the second trip.

Based on the results and observed clusters of neodymium occurrences it was possible to estimate the appropriate GSD to effectively capture reasonably sized clusters. The GSD is important as the occurrences of neodymium are small and can easily disappear if the pixels are not true neodymium pixels. The intention was to estimate the minimum viable cluster size that could fit in one pixel. The estimated GSD required not to lose too much neodymium clusters, was calculated to be 0.6 cm. This was based on counting the pixels across clusters that we perceived to be a minimum size.

The first wall we scanned is located at the east side of the quarry and faces east. This was ideal since the sun illuminates the wall in the morning. “wall6” as it will be referred to, was scanned quite close to the rockface as the rig had to stand on a road. Here, a total of five scans were performed of the wall from a distance of 10m. The lens is made for a minimum of 12 meters, so the images might be prone to some distortion and less sharp resolution.

There was an area on wall5 that looked interesting, but it would’ve been too high up to be captured by the camera if we had done the same setup as the other walls. Therefore, we positioned ourselves obliquely to the interesting area which allowed us to scan it. However, to capture the interesting area, the distance to the wall had to be bigger. Here, four scans were performed.

Wall1 had two set ups, with 10- and 15-meters distance to the rock face. It got scanned four times in total. Wall2 was scanned six times from two separate distances same as wall1. While wall3 was scanned two times from a long distance, about 20 meters.

3.6 Data Processing

Since there are so many corrections for tuning the camera, one needs all the specifications when processing the raw data. Therefore, an in-house software by NEO “HySpex RAD” was used to process the “raw data” into radiance. The process of creating a reflectance image is done by averaging the pixels that show the white reflectance panel, and dividing every image pixel by the average. Atmospheric correction of the field data was not performed as the distance from camera to the quarry face was considerably small and the atmospheric affects were considered to be negligible. To counteract the possibility of the lab data becoming too big for our computers to handle, the process of binning two and two bands was added in the transformation process of the VNIR-3000 data.

The first thing we had to do was transforming from radiance to reflectance, which was done using the calibrated white reference panel and the known absolute reflectance of the panel delivered by the supplier. All the images were processed using the formula below: where F_j is the corrections factor, p_j is the average values for the true reflectance on the WR and avg_j in the average values of the WR in radiance.

$$F_j = \frac{p_j}{avg_i}$$

For implementation purposes we created a python tool that did this operation. It allows the user to mark the four corners inside the WR, and then averaging all the pixels within the selected area. It then multiples the correction factor to all the pixels in the image, writing a new file with identical dimensions, and the new pixel values. It also creates a new “.hdr” header, which is based on the original.

One can also visually inspect the distribution of the correction graph to see if there are any abnormalities (Figure 21 & Figure 22).

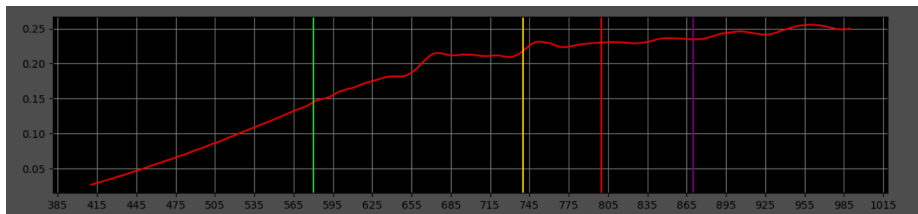


Figure 21: Example of the distribution we hoped to see

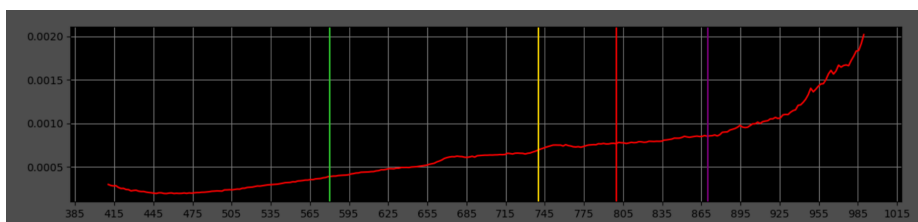


Figure 22: Example of the distribution when something has gone wrong. Typically if areas outside the WR has been included

This helped a lot when converting all the data from radiance to reflectance, as one could spot early if something looked incorrect.

3.7 XRF Lab [5]

To validate some of the observations made in our program, measurements were done with the XRF on a selection of the samples. However, as it is a handheld instrument and the areas of interest are small, a rig was created to allow for more accurate and stable scanning (Figure 23). The rig was set up in a way that allowed for the XRF to be stationary, while the samples could be moved around. The samples were placed on a flat piece of wood that could be raised and lowered in three corners. This allowed the samples to rotate in such a way that the XRF could scan most if not all surfaces.

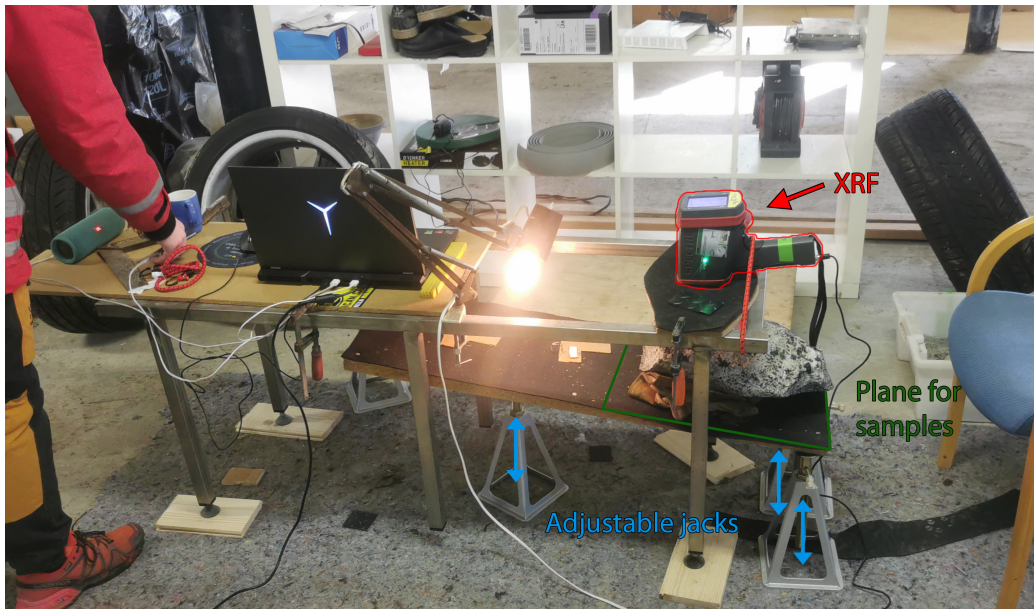


Figure 23: Homemade XRF rig

To choose what areas to scan, we used an early version of the output from Hylite classification. In these rasters we checked if there was a found peak at 580nm, 740nm, 800nm and 870nm; and then the depth was used for the pixel value as a proxy for concentration. For each of these absorption feature locations we have a raster that has values of zero when there is no found feature near the absorption feature location, and the found feature's depth as a value if found. All four features' rasters were written to an hdr file with four "bands", one for each absorption feature. We used the feature depths of the feature around 800nm, and this "band" was used as the displayed band for

not only red, but green and blue, resulting in a grayscale image (Figure 24a). The grayscale image could then be used to find the most interesting areas to measure on the samples. As the overlay was not yet implemented in our in-house software HyperAnalysis (section 4), the image coordinates were used to find the same area in the original image (Figure 24b) which in turn was used to find the same location on the physical stone. Two samples were measured with the XRF using this way of locating promising areas, p1 and p4.

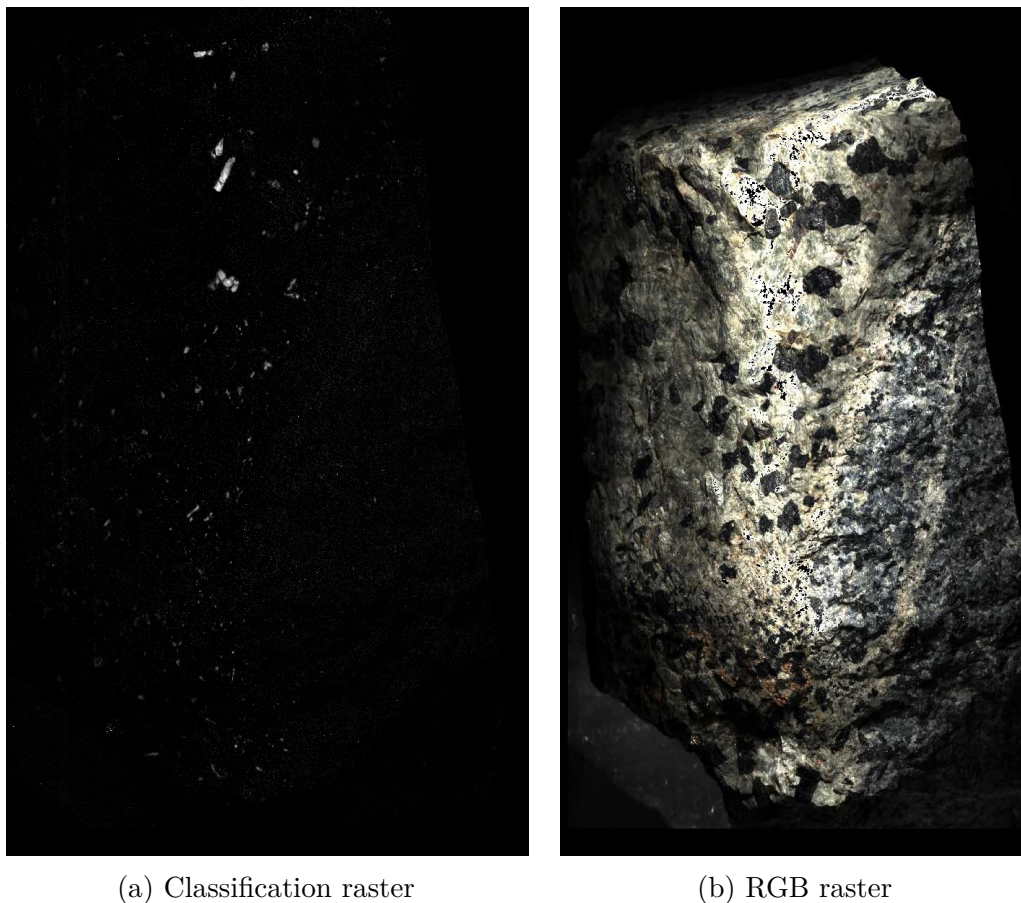


Figure 24: Early version of classification raster and RGB raster of sample P4

4 Software Development

We created our own GUI software called HyperAnalysis for visualizing and interacting with the hyperspectral data. There are some preexisting actors on the market for this purpose, but they tend to be quite expensive and usually each of them have their own complications. Some of the main actors are ENVI, Erdas Imagine, PCI Geomatics and Ecognition. The prices for these solutions are around 100 000 NOK as a single fee, or several thousand NOK a month. For the objective of this sort of process, many of the features in existing software become redundant as well. We focused on the viewer having a low impact on system resources and a high ease-of-use. The software is developed in its entirety using the programming language Python, version 3.8.11.

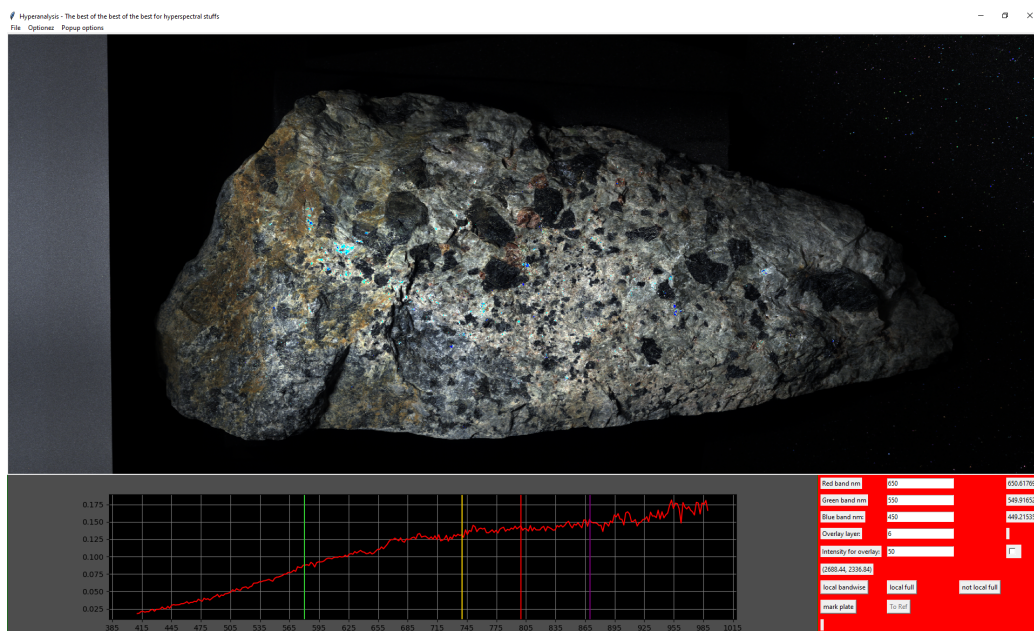


Figure 25: Graphic user interface of Hyperanalysis

4.1 The functionality of HyperAnalysis

Foundational python packages

HyperAnalysis is written entirely in python using the following packages:

Spectral Python (SPy)

Spectral Python is an open-source Python module that is used for processing and reading hyperspectral image data. SPy can read both information from the hdr header and the image data itself. It is also able to save images to the hdr format. (Boggs 2022)

Tkinter

Tkinter is a Python binding to the Tk GUI toolkit. It is the most used GUI for Python and is included in standard python installs.

Pillow

Pillow is an open-source Python module for image processing and visualization. It has a wide selection of processing functions and image manipulation capabilities. (Kemenade et al. 2021)

NumPy

NumPy is a library with support for large multidimensional arrays and a large assemblage of mathematical functions that can do operations on the arrays. It is one of the most used Python libraries and its collection of functions is quite comprehensive. (Harris et al. 2020)

Matplotlib

Matplotlib is a library for plotting and visualization in python. This is also a comprehensive library and adds the possibility of embedding plots into GUI toolkits like Tkinter, which is the one used in HyperAnalysis. (Caswell et al. 2021)

Functionality walk-through

When you open an image, whether it is to be viewed, for reference or as an overlay, the entire image is read into a NumPy memmap object. Memmap is short for memory-map, meaning that the image data is not fully read into memory by python but instead mapped to the binary ".img" file on disk.

The memmap is good for accessing small segments of large arrays without flooding the memory. The reason for loading the data into a memmapped array is that each of our images usually range from around 8–30 GB and in the software, we will mostly either look at full spatial resolution with 3 bands or a single pixel with all bands. This makes reading the entire image into memory unnecessary as it causes slowdowns and is wasteful of computational resources.

For the displayed image, a subset with three bands is extracted from the larger memory mapped array based on the selected wavelengths for red, green and blue. If an overlay is loaded and active, its values are added to the red channel in this array. The equalization is also done on this extracted array. The equalization is in essence normalizing the values to have a minimum of 0 and a maximum of 1. The different equalizations are whether to normalize the part of the image that is visible or the entire image, and whether to normalize the bands individually or as a group.

After the array has been processed, it is converted to an 8-bit integer representation and then used to create a PIL Image object. The PIL Image object is used for spatially manipulating the image. Spatial manipulation of the image is done by an affine transformation using an affine transformation matrix. The affine transformation matrix is changed by the user input in a way that translates to spatial movement of the displayed image.

The affine transformation matrix is also used to translate the mouse coordinates to image coordinates. Image coordinates are used for getting specified parts of the image data array. For the plot, the mouse coordinates are translated to image coordinates and the spectrum of that point is extracted from the memmap before being passed as y-data to the plotting function. They are also used directly and continuously for the image coordinates display in the GUI. To mark the calibrated white reference panel for converting from radiance to reflectance, you click a button that records the next four clicks as you mark the corners. The marked corner coordinates are used to get indexes of the smallest enclosing rectangle within them. These rectangle indexes are then used to get the mean of the WR spectra before being passed to the function that does the converting.

4.2 User Interface

HyperAnalysis

The interface is made up of four main elements; 1, the menubar at the top; 2, the main image viewing window; 3, a spectral viewer in the bottom left; 4, an options menu in the lower right. (see Figure 26)

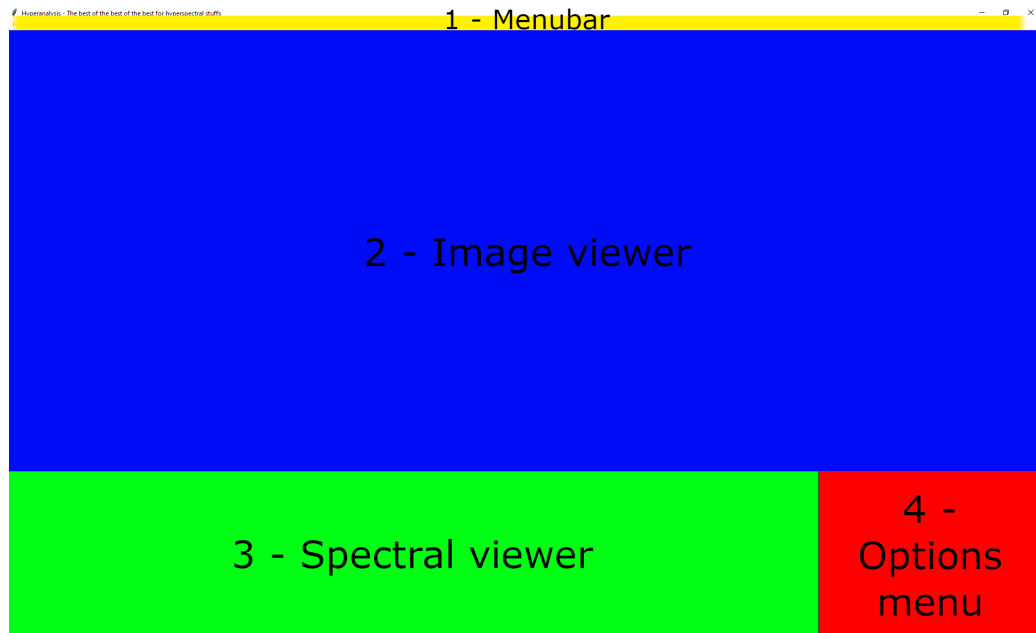


Figure 26: User interface of Hyperanalysis

The main function of the program is to be able to open and view hyperspectral images and plotting their spectra. It's possible to get the spectrum from one image and display another. You can also overlay a band from one file on the original image.

Images are opened through the menubar at the top, which are then displayed in the image viewer. From here you can also open a separate image for the spectral viewer or an image for overlay, the images would have to have the same spatial dimensions. This was necessary for being able to view the actual spectral signatures when viewing a classified image, which is void of any spectra. When you left click in the image viewer, the plot in the spectral viewer changes to the spectrum of the pixel you clicked. The rest of the

controls are regular image-viewer controls with left mouse hold for panning and mouse wheel for zooming.

In the option menu on the lower right there are some options for the displayed image. You can choose what wavelengths in nanometers you want to be represented as red, green and blue and it will get and display the bands closest to the selected wavelengths. There are some options for equalization where you can use min and max values from either the viewable outcrop, or the full image. The image coordinates are displayed continuously for where the cursor hovers. There is an input option for overlay intensity accompanied by a checkbox for toggling the overlay. This is also where you mark the calibrated white reference panel in the images and consecutively convert them from radiance to reflectance.

In the top menubar you have some more functions and options. This is where you open the file to be viewed, the file for the reference spectrum and the file for the overlay. There are options for setting an image rotation and a plot kernel size. The plot kernel size averages the data for the plotted spectra using a specified number of values surrounding the clicked pixel. You have some popup options for smoothing the plotted spectra and another one for options regarding the conversion from radiance to reflectance.

The options for converting from radiance to reflectance involves setting certain parameters that can vary from image to image. You need to set the no-data value, a specified value for pixels that are oversaturated. You also need to set the number of bytes per value in the file, dependent on the file's datatype. The last of the options is setting what calibrated white reference panel was used.

4.3 Hyperspectral Data Analysis - Hylite

Hylite (S. T. Thiele et al. 2021) is an open-source python package for processing and analysis of hyperspectral data. It has a function called “minimum_wavelength” (MWL) that performs a mapping of spectral absorption features. The MWL function performs operations on the data in stages. It starts by flipping the spectrum upside down such that absorption features become peaks, estimates the most prominent peaks and then tries to fit a gaussian curve to these estimated peaks using least squares.

We deliberately chose Hylite over i.e., deep learning to be able to supervise and understand all the steps of the classification. The lack of sufficient training and validation data would in any case have made deep learning challenging. As Hylite is open source, it is possible to dive into the code and both understand it and modify it as necessary. It avoids dealing with an unknown black box and we can more easily understand our classification results and interpret them.

4.3.1 Richardson-Lucy deconvolution

Based on some previously conducted studies, we initially tried to implement Richardson-Lucy deconvolution (R-L deconvolution). R-L deconvolution was originally used to restore blurred images but can also be applied to electromagnetic spectra as a tool for making the absorption features more pronounced. “This specific high pass technique mainly sharpens absorptions, such as those from rare earth bearing minerals, and simultaneously preserves the shape of broader absorptions or the albedo.” (Boesche et al. 2015). We managed a rough implementation but found it to be unnecessary for our data, given the fact that at the time we only had usable data from the lab where we saw clear neodymium correlated signatures. This could however be a useful tool for finding features in the field data.

4.3.2 Hylite Classification Process

The first step to the classification is loading the imaging data into hylite’s data object, HyImage. HyImage is a derived class of the base class HyData. The HyImage/HyData class stores the hyperspectral image in a numpy array, where the dimensions correspond to (rows, columns, bands). The data classes have a lot of methods for manipulating the data, retrieving information and visualizing in the form of simple plotting methods.

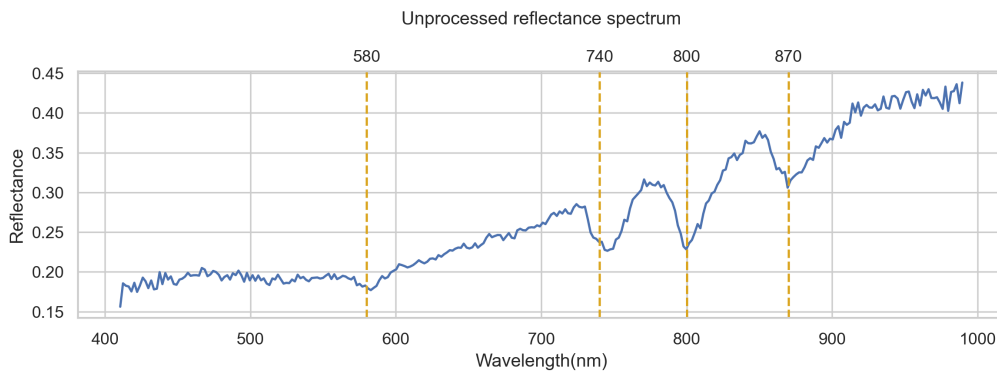


Figure 27: An unprocessed reflectance spectrum from a strongly correlated neodymium pixel

Before passing the data cube to the MWL function it needs to be smoothed to avoid noise interfering with the results. We used a smoothing filter called the Savitzky-Golay filter. The Savitzky-Golay filter aims to maintain sufficient precision of the received signal while not being influenced by noise. We are looking to find absorption features that are quite large in relation to the smaller internal spectral variations. This internal variation can both be real variation in reflectance, or noise. As we are looking for these wider features smoothing will make the slightly larger trends more noticeable.

For the Savitzky-Golay filter, least squares is used to find coefficients that are applied to surrounding values in spectra. The coefficients are dependent on two parameters, window length and poly order. Window length describes the number of surrounding values to use for each value in the spectrum. Poly order is the degree of the polynomial used to fit the samples. The filter is applied through convolution and moves through the spectrum of each pixel computing a new value using the computed coefficients. We smoothed our

spectra using a window size of 23 and a poly order of 2. The smoothed output of the spectrum in Figure 27 can be seen in Figure 28.

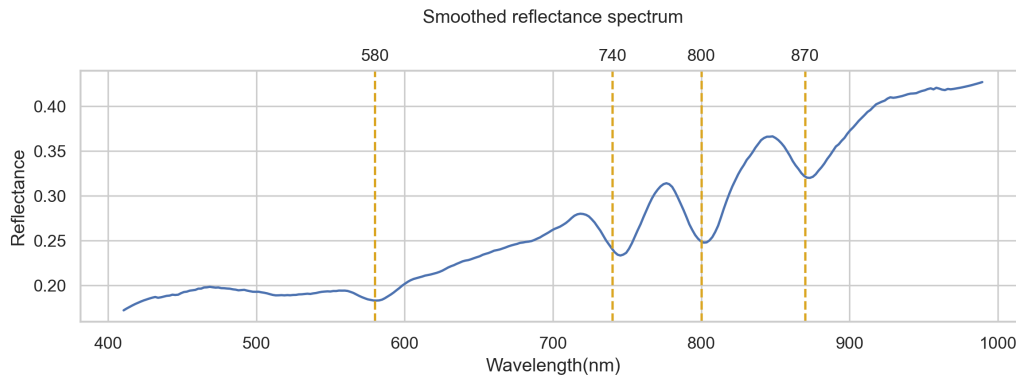


Figure 28: The spectrum in Figure 27 after applying the Savitzky-Golay filter

The first step of the MWL function is to perform a hull correction. The objective of the hull correction is to remove the generalized trend of the whole spectrum, such that if it was completely featureless, it would be a straight line at $y = 1$. The hull correction in Hylite is performed per pixel. The function splits the spectrum into segments recursively based on the deviation from the estimated generalized slope for the whole given segment. Each segmented part of the spectrum is then corrected using the slope and initial value of the segment.

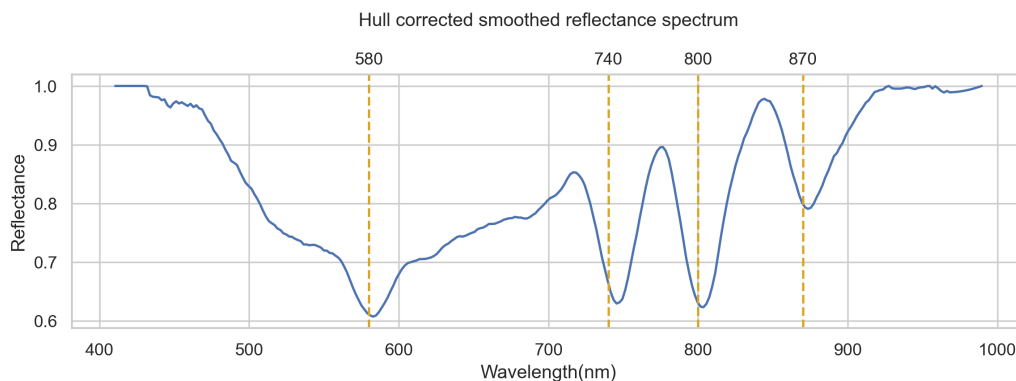


Figure 29: The spectrum in Figure 28 after applying hull correction

When the data has been hull corrected, it is ready for the wavelength mapping. First the spectrum is flipped upside down by subtracting 1 from the whole spectrum. This is done as the internals of the MWL function is made for finding maximums. We are looking to find the most pronounced absorption features, so in flipped data this equates to the most pronounced maximums or peaks.

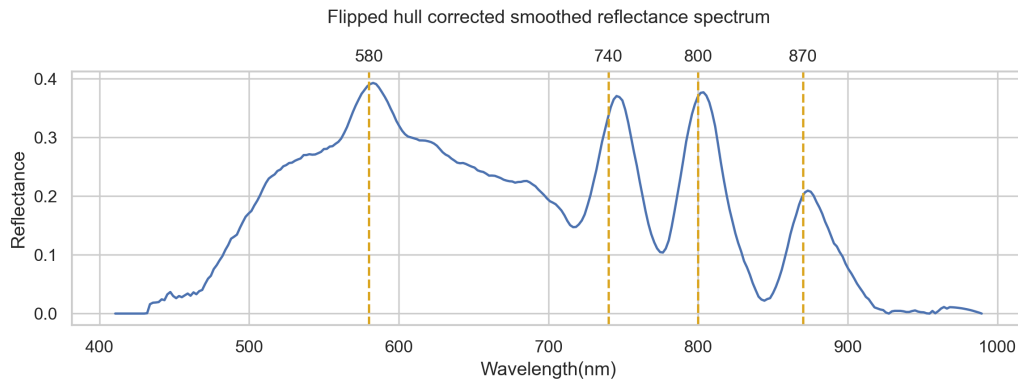


Figure 30: The spectrum in Figure 29 after flipping the spectrum upside down

The last step of the function is finding the absorption features. After flipping the spectrum upside down, we are now looking for the largest peaks in the data. Finding the largest peaks is done by fitting gaussian curves to the data using least squares. Before fitting the gaussians using least squares, we need to find initial guesses. The function goes through each point on the spectrum successively. First it checks if the point is a local maximum by checking that the two points beside it has a lower value than the point itself. Then it checks if the points beside these points are lower and so on. The number of points that are checked is a parameter of the function. For our mapping we checked four points on either side. If the point is deemed to be a local maximum, the height of the feature is evaluated against previously found maximums on the given spectrum. As we are looking for neodymium's four absorption features, we are left with the four highest peaks on the spectrum. The output consists of the peak location, height and widths for all four peaks. This is now our initial guesses for the least squares. After the initial guesses the output results are refined in the least squares analysis.

4.3.3 Hylite Modifications And Output

Hylite comes with support for multiprocessing for the minimum wavelength mapping, but we found that the built-in multiprocessing resulted in unproportionate memory usage and eventually returning memory errors. The memory errors still occurred when the computer used for processing was upgraded from 64gb to 128gb of memory. We then implemented a simpler way of multiprocessing where we split the arrays on the “column”-axis into (number of threads) smaller arrays. I.e., given an image-array of dimensions (10, 300, 300) and 30 threads, the array would be split into 30 image-arrays of dimension (10, 10, 300) or (10, 300/30, 300). After the mapping we are then left with (number of threads) arrays that are merged on the same axes. This can be done without influencing the results, as all the mapping operations are done on individual spectra.

After the mapping has been done and the resulting arrays have been merged back together, we are left with the completed output array that has the same spatial dimensions as the original image. Per pixel the output from the function contains the four largest peaks found. For each of these peaks we have the depth, location in nm, and their width.

Different combinations involving presence of a found peak at neodymium's absorption feature locations and their depth was used to create the classification raster. To be able to easily implement an overlay and visualization into HyperAnalysis, the classification raster was written to an .hdr file. The classification has the same spatial dimensions as the image, while the bands are different ways of visualizing the result. Different ways of visualizing the results are different combinations of where peaks were detected and weights for their depths. The combinations we used the most was one where all peaks had been found, and one where all but the 580nm feature were found. The HyperAnalysis overlay is visualized in Figure 31.

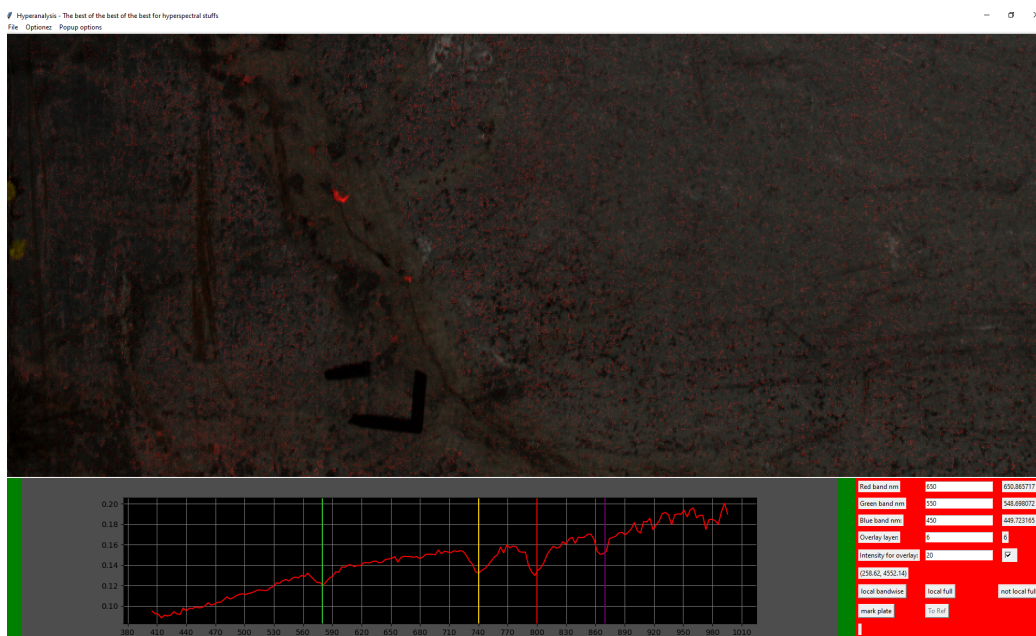


Figure 31: Classification overlay in Hyperanalysis

5 Results

The following chapter will go through the results found by using the above-mentioned methods. The results will be presented consecutively. The structure is chronological since the results rely on each other.

5.1 Initial Field Exploration (XRF) [1]

To be able to proceed with the thesis, the presence of neodymium in the quarry walls needed to be verified. Based on the work done in the thesis of (Herrmann 2019), we know that neodymium's absorption features can be detected in homogeneous powders at a concentration of 0.1% or 1000ppm. Supplementary, according to the work of (Rowan, Kingston, and Crowley 1986) neodymium has the possibility to be detected on fresh rock surfaces with concentrations as low as 0.03% or 300ppm. The XRF handheld detected amounts of neodymium concentration on the wall, with most measurements being above 300ppm and a couple around 1000ppm. It should be noted that the standard deviation calculated by the XRF is quite high for most of the samples, but the overall neodymium concentration results seemed sufficient for proceeding. Table 4 shows the XRF results from measuring the 14 points on the wall and 3 points near a ledge. NA in the table Table 4 are where the XRF didn't output a standard deviation.

Point [sample-n_scan-duration]	Measured value [ppm]	Standard deviation [ppm]
p1-1-60	528	416
p1-2-30	617	307
p1-3-10	1018	411
p1-4-60	464	438
p2-1-60	294	NA
p3-1-60	378	NA
p4-1-60	323	NA
p5-1-60	349	258
p6-1-60	1076	258
p7-1-60	408	299
p8-1-60	685	268
p9-1-60	288	NA
p10-1-60	985	749
p11-1-60	360	NA
p12-1-60	523	355
p12-2-60	459	328
p13-1-60	272	NA
p14-1-60	585	454
p15-1-60	470	NA
p16-1-60	285	NA
p17-1-60	414	276

Table 4: XRF measurements from the field exploration

5.2 First Quarry-Scan [2]

The data from the first field data collection in December presented some challenges. A systematic flaw with the data, after at-surface-reflectance retrieval, was discovered. After transformation of the data from radiance to reflectance, the correction graph is shown in Figure 32.

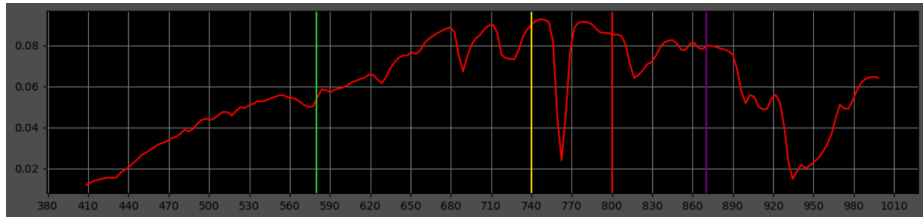


Figure 32: Image of the systematic flaw in the reflectance data. The dip around 760nm was prominent in all pixels.

This differs from the expected spectrum, which is usually a gradual descent. The field work was performed in December under low sun angles, low illumination and snow covering the ground. It is natural to suspect that the snow interfered with the sensor somehow. A theory is that the light from the sun got reflected from the snow, and onto the camera and the WR. This could result in too many light sources causing stray light to interfere in the correction (Widén and Munkhammar 2019).

The purpose behind the lidar data acquisition, was to investigate whether it could be used to help with the classification. The idea was to use the microgeometry from the lidar data and see if it correlated with neodymium. However, we decided that it was complex and not worth the hassle since the image data alone gave good results. It was used as a visualization of wall 1 and used when estimating the shadow angle in the quarry.

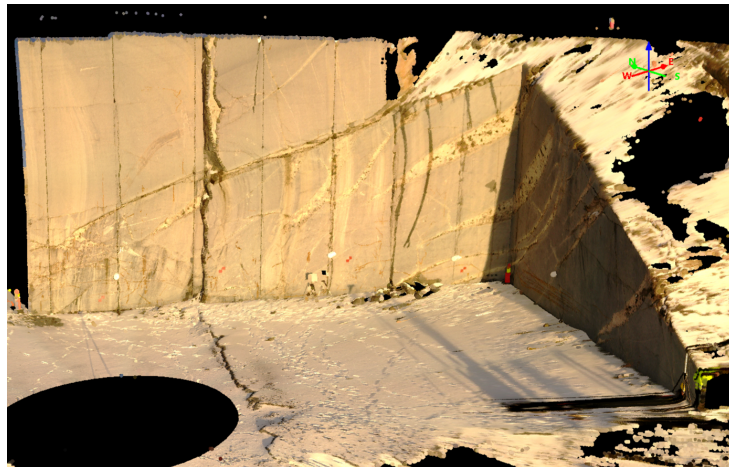


Figure 33: Lidar point cloud from wall1

5.3 Lab Samples [4]

When examining the sample scans, a quite pronounced, almost exemplary, neodymium signature was found by clicking around in the image of sample p4. A number of these distinct signatures were found when manually exploring the sample data. A log with coordinates over interesting areas that showed promising spectral attributes was created. The log was used as validation for hylite, and to show interesting areas for the XRF lab.

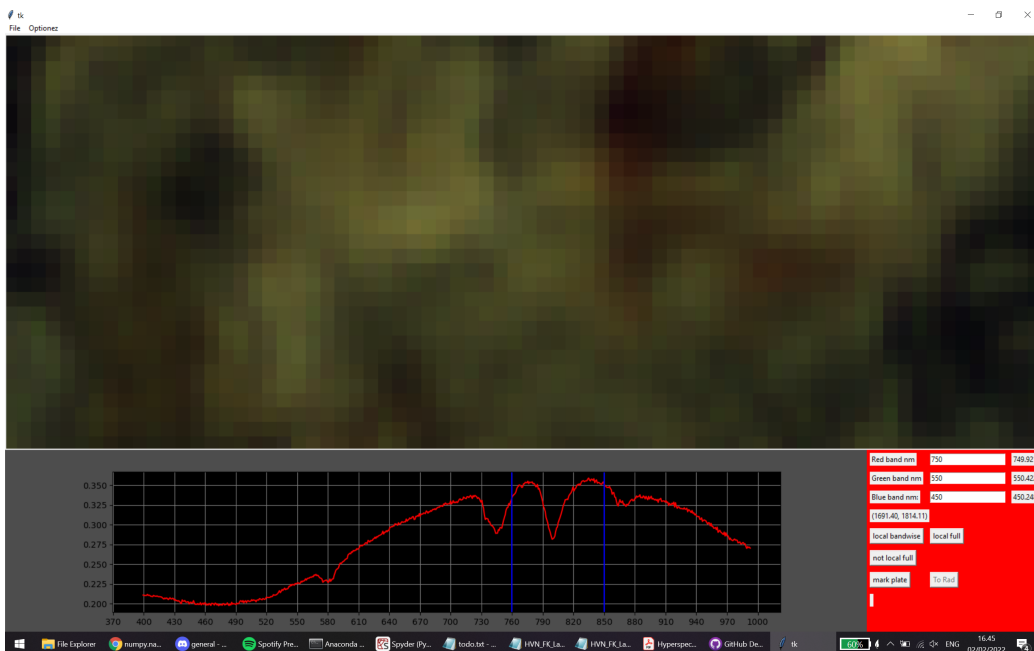


Figure 34: Neodymium spectrum identified by clicking in the image.

Hylite mapping produced raster datacubes with the four deepest found features and their depths for each pixel. Initially we used the depth of the feature around 800nm, if it was found, to create a raster. We saw clear neodymium signatures in all the samples but will explore and visualize P1 and P4 in more detail.

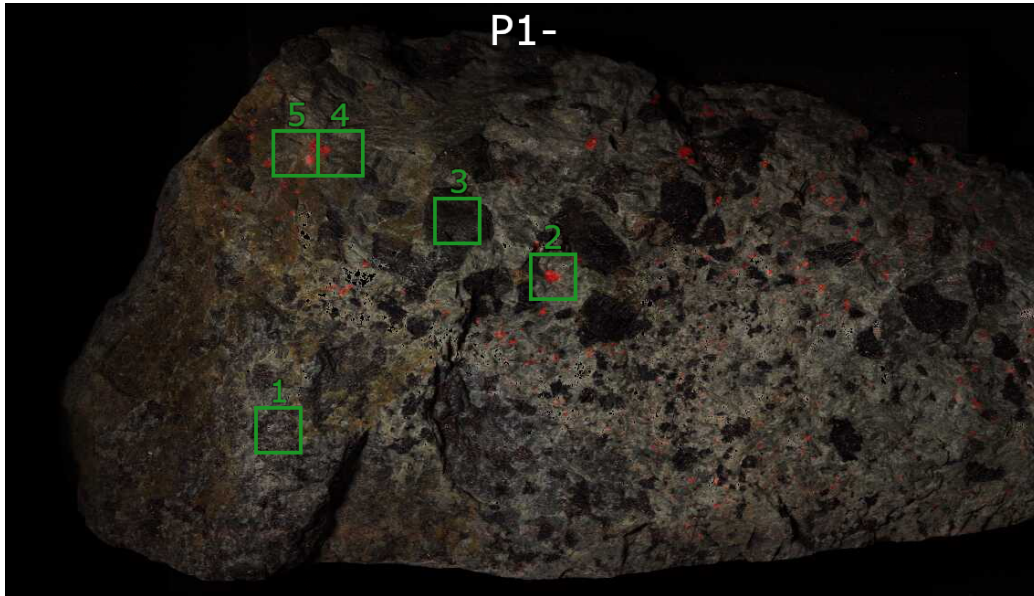


Figure 35: Areas on sample P1 that have been classified and scanned with the XRF. See Table 5

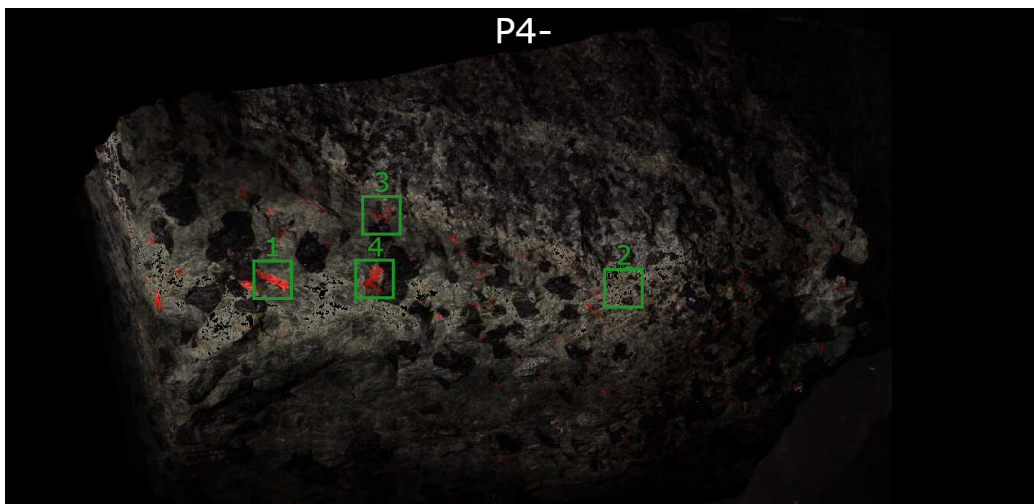


Figure 36: Areas on sample p4 that have been classified and measured with the XRF. Area 2 and 3 has not been measured with the XRF.

The 800nm feature depth raster proved itself to be good indicator for neodymium signatures. For the brightest areas, the ones with the deepest 800nm feature, you can clearly see all the absorption features in the reflectance spectrum. We found that the clustering of pixels with a mapped 800nm feature was an indicator that the pixels in the cluster represented the neodymium signature. This is an important factor to consider in relation to choosing a reasonable pixel size for scanning in the field for this type of pegmatitic rock. The spectrum below illustrates the pronounced features found in a pixel with a deep 800nm feature from area P4-1 in Figure 37.

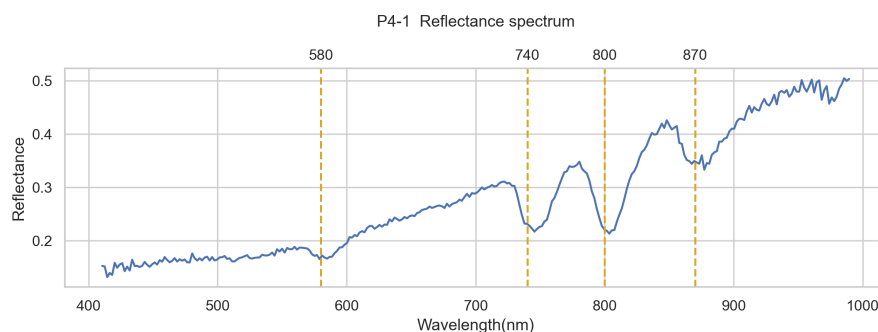


Figure 37: Unprocessed reflectance spectrum from a pixel in the area P4-1

Moving to a shallower found feature in area P4-2 from Figure 38, the features are getting less pronounced. It's still quite clear that there are features at 740nm, 800nm and 870nm. The feature at 870nm is shallower than the 740nm and 800nm, but more noticeable than the 580nm feature that is starting to disappear.

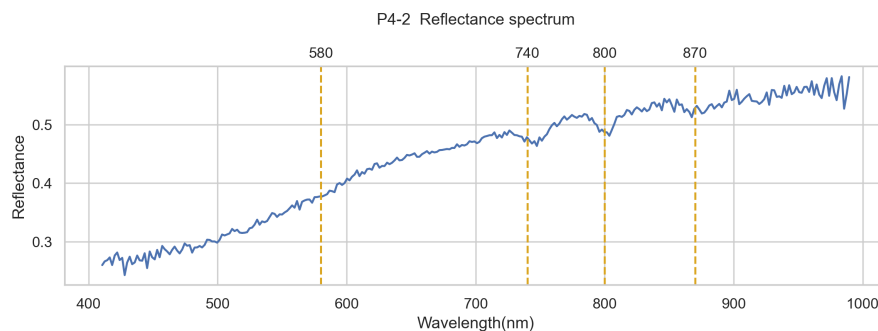


Figure 38: Unprocessed reflectance spectrum from a pixel in the area P4-2

Area p4-3 has two clusters of 800nm features and the spectrum from this area is taken from the outskirts of one of these clusters. It is hard to see any neodymium indicators in the reflectance spectrum of this pixel. But after the spectrum has been smoothed by the Savitzky-Golay filter the features start to appear. In Figure 39 the significant variation in the spectrum is visible but there are some signs that the features are present. The features could be due to noise, and it's hard to verify the presence of Nd. The spectrum in Figure 40 is most likely Nd as this particular pixel was in the outskirts of a cluster that had deeper features near the center. It is not an obvious neodymium signature, but the tendency is there.

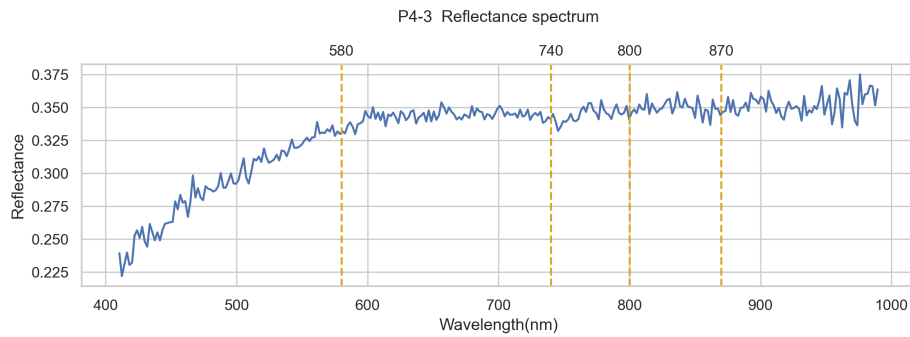


Figure 39: Unprocessed reflectance spectrum from a pixel in the area P4-3

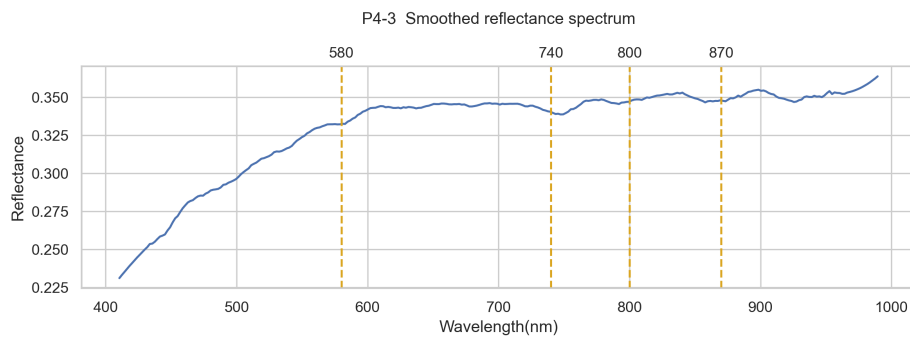


Figure 40: Smoothed reflectance spectrum from a pixel in the area P4-3

5.4 Lab Samples XRF Validation [5]

For verification of the areas with signatures resembling that of neodymium, XRF measurements were taken. Some of these areas were measured more than once, as the XRF is difficult to aim at a specific location. The results show that there is a correlation between the observed neodymium spectra and a presence of neodymium. We can also see the tendency of correlation between depth of the features and neodymium concentration, also described in the thesis of (Herrmann 2019). Table 5 below describes the largest measured concentration of neodymium in each point and their standard deviations. The point locations on the samples can be visualized in Figure 35(sample P1) & Figure 36(sample P4).

Sample	Image ref Fig 35, Fig 36	Image coordinates (x, y)	Largest value [ppm]	Standard deviation [ppm]
P1	1	543, 717	493	NA
P1	2	1043, 1626	445	257
P1	3	1225, 1321	272	NA
P1	4	1414, 842	6952	346
P1	5	1448, 895	1471	255
P4	4	1531, 2718	72969	3061
P4	1	1538, 2180	23445	1331

Table 5: XRF measurements done in the XRF lab

5.5 Second Quarry-Scan [6]

As the XRF lab results indicated a strong correlation between the classified areas and the points with high concentration, it gave the foundation to do the same classification of the field data. When exploring the field data, reflectance retrieval showed good results, apart from a strong oxygen feature present in the data around 760nm. The estimated required GSD was roughly 0.5cm. However, not all the scans were taken within this requirement. For this section, four walls in the main quarry are highlighted, excluding details on wall6. The classification from wall6 did show promising results, with a few clusters of spectral signatures indicating presence of neodymium.



Figure 41: RGB image of wall1



Figure 42: Example area of classification overlay of wall1 in Hyperanalysis

We observed the same tendencies on the walls as we did in the lab data. The outcrop is from one of the areas with both the highest number of found, and the most pronounced neodymium spectra on wall1. This was the true for all images, however the strength of the spectral signatures varied.

Figure 43 shows point spectra from the four walls. We decided to group these four walls as they represent the same area. These are the non-smoothed spectrum data and can therefore be harder to interpret. The spectra from Wall1 and wall3 are the ones that most and least resemble the Nd spectral signature. Wall1 is the wall that we put the most focus on, and the only wall where we collected XRF data. The pixel chosen for the plot shows a prominent neodymium spectrum. And when compared to wall3, where the features disappear in the noise it is reasonable to think the concentration to be lower. However, wall3 was scanned from a further distance and with a different lens. It has in general less prominent features, which are to be expected due to lower energy, and that the pixel not “pure” neodymium pixels. Based on wall3’s raw spectrum, little to no neodymium features are shown.

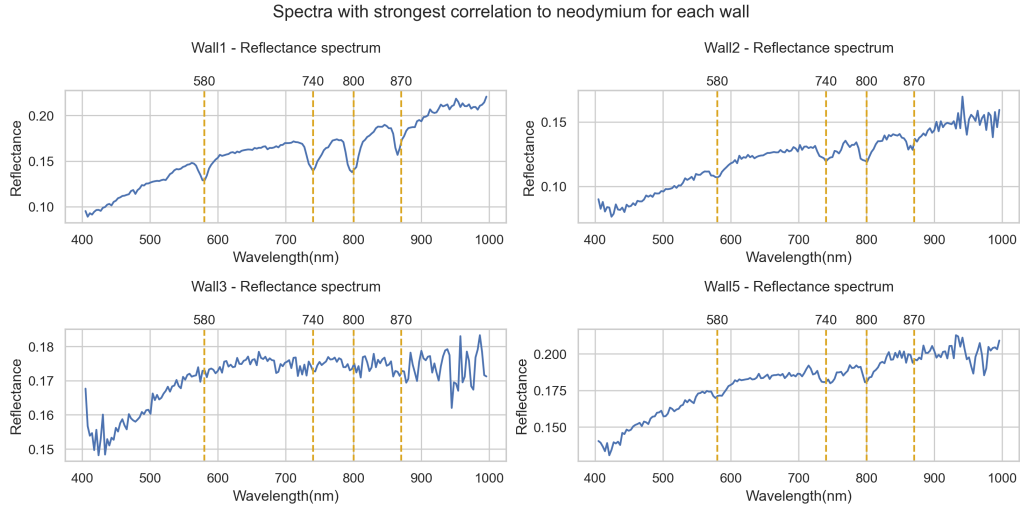


Figure 43: Spectra that strongly correlates with the known neodymium features: 580nm, 740nm, 800nm and 870nm.

A very important aspect when interpreting these data is to take geometrical and spectral resolution into account. In our field study, state of the art cameras were used. They have incredibly low spectral and geometrical error, with a very low PSF, SRF, smile and keystone. The reason this is very important in these classifications is because the Nd occurrences are so small. The areas of interest (minerals) can be as small as 0.1 cm^2 , and it is therefore crucial that the camera is able to map these occurrences correctly in each pixel. If pixels were to leak spectral and geometrical attributes unto the neighboring pixels, pixel-based classification would be impossible. This would not be as important if the areas of interest were significantly bigger than the GSD, where the neighboring pixels would contain more similar values.

The Figure 44 shows spectra with shallow features, collected from all the four walls. These are spectra that correlate with neodymium’s spectral signature, but the depth of the features are shallow compared to the deepest found features. These are pixels which probably has some neodymium in them but might not be pure pixels. These are the most typical spectra we observed that we assume to be neodymium.

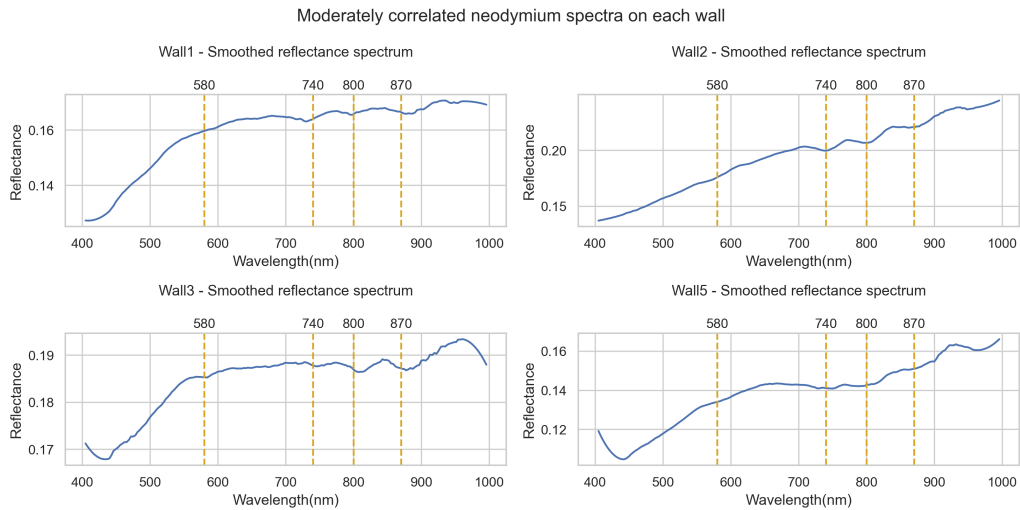


Figure 44: Spectra that somewhat correlates with the known neodymium features: 580nm, 740nm, 800nm and 870nm.

As seen in Figure 45 there are many pixels which are hard to define. A weakness for our study is the lack of conclusive validation data. These are all spectra which, to some degree, show absorption attributes of neodymium. However, they are not like the ones observed in the lab. Based on (Herrmann 2019) measurements can be strongly affected by the surrounding minerals and Nd features might be imprinted onto other existing mineral spectra and spectral trends. It is therefore possible to see Nd absorption features, but close to impossible to accurately estimate the Nd concentration in field. It was also indicated that irons spectral response (wide, shallow features around 650 and 900nm) suppresses that of REEs. More information would be needed to make assumptions regarding the concentration of neodymium.

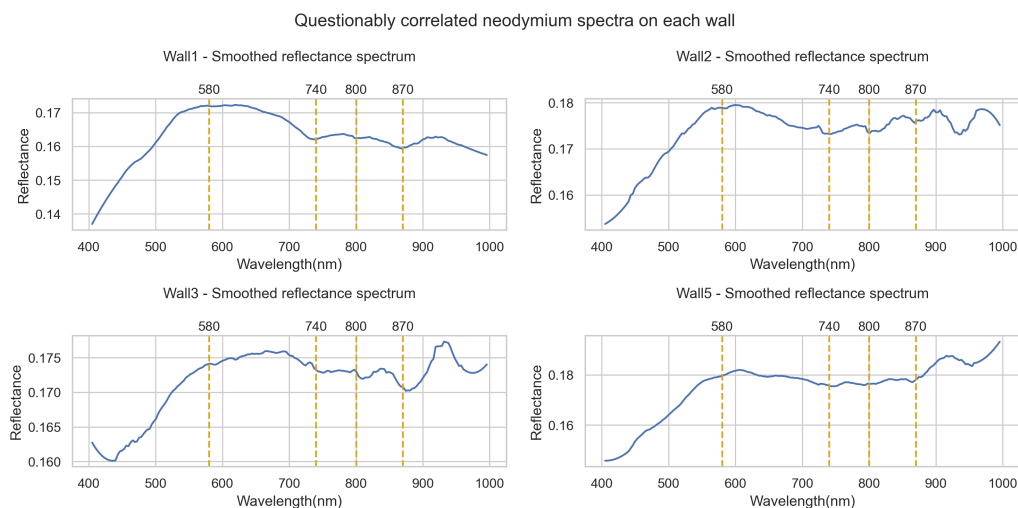


Figure 45: Spectra with low correlation to the know neodymium features, and are therefore hard to classify.

5.6 Processing

Processing time and big-data handling are important aspects when looking at the possibility of streamlining the mapping process. The CPU's number of threads and clock speed dictate the processing speed. The way the mapping is implemented now, a certain amount of RAM is required for the analysis to run, dependent on the size of each file. From observing the resource usage for our images this seems to be in the ballpark of around 50-60GB. This can easily be modified for less memory usage at the potential cost of increased processing time. One way of doing this would be to do the analysis batchwise on each image, i.e., splitting the image into two smaller images, running the analysis on them successively, and then merging them back together.

The way we implemented Hylite multiprocessing also means that this could be scaled to maximize usage of computational resources given a higher data load. This could be scaled up for both several separate computers and larger clusters of hardware. The processing setup is also quite trivial to implement in a cloud service like Amazon Web Services, where the data could start processing right away when it's added to some cloud storage.

We logged the processing time of each thread for a batch of images. The processing times for a batch of 20 images relative to their file sizes are visualized in Figure 46 below. The computer used for processing has high-end components that aids in reducing the processing time. The relevant computer specifications can be seen in Table 6. A linear trend between processing time and file size is visible. There are small variations from the linear regression line, and these are most likely due to variations in clock speed and potentially the number of iterations in the least squares refinement.

This points to the method being highly scalable and can easily be made to handle larger computer clusters with more threads.

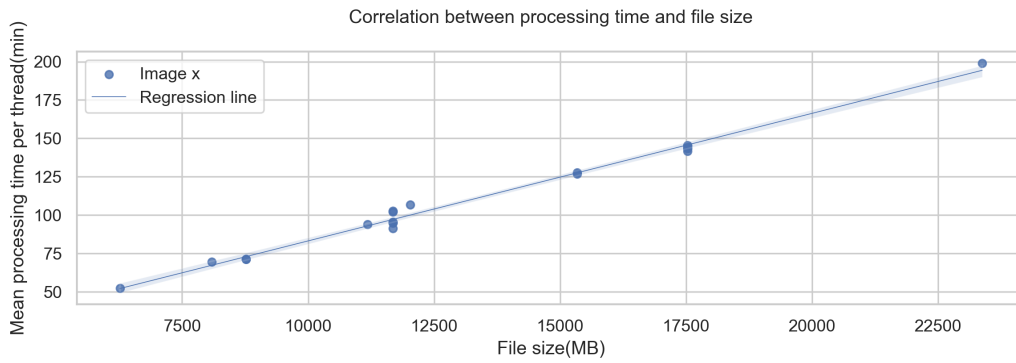


Figure 46: Correlation graph between processing time and file size.

Component	Specifications
CPU	16 cores, 32 threads Base Clock: 3.5GHz, Max. Clock: 4.7GHz
RAM	128 GB, DDR4, 3200MHz
SSD read/write speeds	Read: 4950MB/s, Write: 4250MB/s

Table 6: Hardware specification for the processing computer

6 Discussion

6.1 Classifications Aspects, Potential For Machine Learning

There are several parts of our classification method that leaves more to be desired, and it has great potential for improvement. A method of looking at more specific absorption features should be developed and implemented. When we look for the four deepest features on the spectrum instead of looking at the features specific to neodymium, information about them can be lost. If there are larger features elsewhere on the spectrum due to noise or other influences, and there exists a neodymium feature, the neodymium feature will be lost. There could still be refinement of the results given our output from the MWL function. One could tweak and implement different approaches, like the presence of a specified number of features instead of specific combinations. Thresholds for the depth of the features is another way of refining the classification results using the method described in this study.

Machine learning also has the potential to greatly increase the classification accuracy. The greatest issue with implementing machine learning is the lack of validated, labelled training data. We have images with low GSD but the clusters of neodymium can be as small as 1cm². To be able to train a decent deep learning model we would need knowledge of the actual neodymium levels in each pixel and not just an estimate. As the neodymium levels can't be measured remotely one would also have to project the results so that they spatially align with the hyperspectral image. The possibility is there but would be quite involved. One theoretical way could be using an XRF device that could be automatically moved and geolocated that would take a very large number of measurements that could be interpolated to a complete raster.

One aspect of implementing machine learning is that one might be able to quantify the neodymium content, given the thesis of (Herrmann 2019). It would be interesting to see i.e., a U-net regression model with good training data. In our data we observed that in the clusters of neodymium, the signature would be more pronounced near the center and be harder to recognize the further from the center. As U-net is a deep learning architecture that keeps in mind the spatial relationship between pixels it might be able to use the

clustering information for better prediction. Combining this with regression means that you might be able to output a continuous raster of neodymium content in each pixel, of course with some uncertainty.

6.2 Can REE Classification Based On Hyperspectral Imaging Be Integrated Into The Mining Industry?

For something to be streamlined, it must be applicable in practice. A major cornerstone of doing any sort of data collecting with a hyperspectral sensor, is to have good weather conditions. Based on our results from being in field, the key difference from the first and second trip was the weather conditions. The first field which was done in December, had sunny conditions but were problematic due to the snow. The second trip also had sunny conditions but were done in March with no snow. It is therefore impossible to compare the two scans, due to the systematic error in the data from the first field data collection. It is therefore unclear whether the sun conditions were good enough in December to do a classification. It would therefore be interesting to do more research into the minimum required sun intensity to capture REEs in field. This would make it possible to estimate the number on potential scan days in year, which would show the potential efficiency of mapping REEs.

The field-rig used in our thesis was a HySpex VNIR1800 on tripod with rotations stages. Since the rig was reliant on a power generator and had to be manually moved the transition time between scans was somewhat high. However, this could easily be streamlined with putting the rig on a vehicle. Each scan took roughly 5 minutes, plus a few minutes of tuning before each scan. With a more effective transition time, it would perhaps be possible to scan 2-3 walls per hour.

7 Conclusion

This study has set out to test whether hyperspectral imagery can be used in a more applicable way in the mining industry. Two main objectives of this thesis were:

- if it was possible to map neodymium in a discontinued quarry in Larvik?
- is it possible to streamline HSI scanning within operating quarries?

The classification results show strong correlation with neodymium features. The measurements from the XRF-rig indicated that the concentration was higher in the areas identified in lab-data. The measurements done in field with the XRF also indicated high neodymium concentrations which supports the classification. The spectral signatures that were identified also showed a big correlation with the spectral signature found in the studies of (Boesche et al., 2015b; Sabrina Herrmann, 2019b). This leads us to conclude that the quarry (“Vevja”) contains minerals with high enough concentration of neodymium to be mapped with HIS. The classification itself is not refined due to lack of validation data, time constraints and the fact that the classification was not the main aim of this thesis. The lack of validation data is also a big reason that neural networks were not used in this study.

With the first thesis question answered, the second question was whether it was possible to streamline the process of mapping and identifying neodymium. Since we did not collect the data without help, the data acquisition part of streamlining the process was just done in theory as there was no possibility of testing out these theories on our own. However, everything from the raw data to the classification was possible to streamline. A major part of this, was creating a program that allowed us to easily process and classify the data. One aspect that was important in the processing and classification, was managing the data size. Since the data size of each image easily exceeded 10 GB, the program had to handle huge amount of data at the same time. Therefore, a lot of effort was put into creating a better multiprocessing procedure and facilitating for scalability. This allowed for quicker classification and made the process doable. The time needed to process each scene was around 1 to 3 hours, which makes the process applicable.

7.1 Further Research

There were many things that could be more refined given more time. Things that we would have done if given more time:

- Collecting more validation data, and perhaps analyse the minerals with electron microscope to verify the content of REEs. And figure out the mineralogy in the quarry. It would perhaps allow for implementing neural networks in some parts of the classification
- Do more research into single image vs averaged images classification
- More research into dealing with big data, Hylite could use some better memory management.
- Refinement of the classification process. I.e, Looking for, and mapping the depth of neodymium's specific features instead of the overall four deepest features.

References

- Bakker, Wim, Harald van der Werff, and Freek Meer (May 2019). “Determining Smile And Keystone Of Lab Hyperspectral Line Cameras”. In: pp. 1–5. DOI: 10.1109/WHISPERS.2019.8921045.
- Boesche, Nina et al. (Feb. 2015). “Hyperspectral REE (Rare Earth Element) Mapping of Outcrops—Applications for Neodymium Detection”. In: *Remote Sensing* 7, pp. 5160–5186. DOI: 10.3390/rs70505160.
- Boggs, Thomas (2022). “Spectral Python (Spy)”. In: URL: <http://spectralpython.net>.
- Boissenin, Clara (2021). “Analysing Critical Incidents for Rare Earth Elements Supply & Use in Europe”. In.
- Booyesen, René et al. (May 2020). “Detection of REEs with lightweight UAV-based hyperspectral imaging”. In: *Scientific Reports*. DOI: 10.1038/s41598-020-74422-0.
- Boynton, W V (Apr. 1984). “Cosmochemistry of the Rare Earth Elements[A]. Ins Henderson P ed. Rare Earth Element Geochemistry”. In: *Developments in Geochemistry[C]*, pp. 3–114.
- Caswell, Thomas A et al. (May 2021). “matplotlib/matplotlib: REL: v3.4.2”. In: DOI: 10.5281/ZENODO.4743323. URL: <https://zenodo.org/record/4743323>.
- Crocombe, Richard, Pauline Leary, and Brooke Kammrath (Apr. 2021). “Portable Spectroscopy and Spectrometry 1”. In: DOI: 10.1002/9781119636489.
- Gao, Bo-Cai et al. (May 2009). “Atmospheric correction algorithms for hyperspectral remote sensing data of land and ocean”. In: *Remote Sensing of Environment* 113. DOI: 10.1016/j.rse.2007.12.015.
- Gao, Zhenyu et al. (May 2016). “Simulation and Analysis of Spectral Response Function and Bandwidth of Spectrometer”. In: *International Journal of Aerospace Engineering* 2016, pp. 1–8. DOI: 10.1155/2016/2759121.
- Gilabert, M A, Claudio Conese, and Fabio Maselli (Apr. 1994). “An atmospheric correction method for the automatic retrieval of surface reflectance from TM images”. In: *International Journal of Remote Sensing - INT J REMOTE SENS* 15, pp. 2065–2086. DOI: 10.1080/01431169408954228.
- Goodenough, Kathryn et al. (May 2016). “Europe’s rare earth element resource potential: An overview of REE metallo- genetic provinces and their

- geodynamic setting”. In: *Ore Geology Reviews*. DOI: 10.1016/j.oregeorev.2015.09.019.
- Harris, Charles R. et al. (Sept. 2020). “Array programming with NumPy”. In: *Nature* 585 (7825), pp. 357–362. ISSN: 0028-0836. DOI: 10.1038/s41586-020-2649-2.
- Heldal, T and Rolv Dahl (May 2013). “Global stone heritage: Larvikite, Norway”. In: *Geological Society, London, Special Publications* 407, p. 11327. DOI: 10.1144/SP407.14.
- Herrmann, Sabrina (2019). “Capacity of imaging spectroscopy for the characterisation of REO, REE bearing minerals & primary REE-deposits”. GFZ German Research Centre for Geosciences. DOI: <https://doi.org/10.2312/GFZ.b103-19089>.
- IEA (2021). *Mineral requirements for clean energy transitions*. IEA.
- Ilankoon, I M Saman K et al. (Apr. 2021). “Constraints to rare earth elements supply diversification: Evidence from an industry survey”. In: *Journal of Cleaner Production* 331, p. 129932. DOI: 10.1016/j.jclepro.2021.129932.
- Jackson, Wayne D. and Grey Christiansen (1993). *U. S. GEOLOGICAL SURVEY CIRCULAR 930-N*.
- Jensen, John R. (2014). *Remote Sensing of the Environment An Earth Resource Perspective Second Edition*.
- Kemenade, Hugo van et al. (Oct. 2021). “python-pillow/Pillow: 8.4.0”. In: DOI: 10.5281/ZENODO.5571504. URL: <https://zenodo.org/record/5571504>.
- Neumann, Else-Ragnhild et al. (May 2004). “Carboniferous-Permian rifting and magmatism in southern Scandinavia, the North Sea and northern Germany: A review”. In: *Geological Society London Special Publications* 223, pp. 11–40. DOI: 10.1144/GSL.SP.2004.223.01.02.
- Rani, Nisha, Venkata Mandla, and Tejpal Singh (May 2016). “Evaluation of atmospheric corrections on hyperspectral data with special reference to mineral mapping”. In: *Geoscience Frontiers* 8. DOI: 10.1016/j.gsf.2016.06.004.
- Reinhard, Erik et al. (Apr. 2006). *03. HDR Image Encodings*. DOI: 10.1016/B978-012585263-0/50004-X.
- Rowan, Lawrence C., Marguerite J. Kingston, and James K. Crowley (July 1986). “Spectral reflectance of carbonatites and related alkalic igneous rocks; selected samples from four North American localities”. In: *Economic Geology* 81 (4), pp. 857–871. ISSN: 1554-0774. DOI: 10.2113/gsecongeo.81.4.857.

- Schowengerdt, R.A. (Jan. 2007). *Remote Sensing*. DOI: 10.1016/B978-0-12-369407-2.X5000-1.
- Shukla, Alpana and Rajsi Kot (Apr. 2016). “An Overview of Hyperspectral Remote Sensing and its applications in various Disciplines”. In: *IRA-International Journal of Applied Sciences (ISSN 2455-4499)* 5, p. 85. DOI: 10.21013/jas.v5.n2.p4.
- Sunde, Øyvind, Henrik Friis, and Tom Andersen (June 2019). “Pegmatites of the Larvik Plutonic Complex, Oslo Rift, Norway: field relations and characterisation”. In: *Norsk Geologisk Tidsskrift* 99, pp. 93–111. DOI: 10.17850/njg99-1-05.
- Thiele, Sam et al. (May 2021). “A Novel and Open-Source Illumination Correction for Hyperspectral Digital Outcrop Models”. In: *IEEE Transactions on Geoscience and Remote Sensing* PP, pp. 1–12. DOI: 10.1109/TGRS.2021.3098725.
- Thiele, Samuel T. et al. (Sept. 2021). “Multi-scale, multi-sensor data integration for automated 3-D geological mapping”. In: *Ore Geology Reviews* 136, p. 104252. ISSN: 01691368. DOI: 10.1016/j.oregeorev.2021.104252.
- Turner, David, Benoit Rivard, and Lee Groat (May 2018). “Visible and short-wave infrared reflectance spectroscopy of selected REE-bearing silicate minerals”. In: *American Mineralogist* 103, pp. 927–943. DOI: 10.2138/am-2018-6195.
- Widén, Joakim and Joakim Munkhammar (Apr. 2019). *Solar Radiation Theory*. ISBN: 978-91-506-2760-2. DOI: 10.33063/diva-381852.
- Xu, Chengjian et al. (Apr. 2020). “Future material demand for automotive lithium-based batteries”. In: *Communications Materials* 1, p. 1234567890. DOI: 10.1038/s43246-020-00095-x.



Norges miljø- og biovitenskapelige universitet
Noregs miljø- og biovitenskapelige universitet
Norwegian University of Life Sciences

Postboks 5003
NO-1432 Ås
Norway